

Hydraulic model calibration using CryoSat-2 observations in the Zambezi catchment

Cécile M.M. Kittel^{1,1}, Simbidzayi Hatchard^{2,2}, Jeffrey Charles Neal^{2,2}, Karina Nielsen^{3,3}, Paul D Bates^{2,2}, and Peter Bauer-Gottwein^{1,1}

¹Technical University of Denmark

²University of Bristol

³DTU Space

November 30, 2022

Abstract

Geodetic altimeters provide unique observations of the river surface longitudinal profile due to their long repeat periods and densely spaced ground tracks. This information is valuable for calibrating hydraulic model parameters, and thus for producing reliable simulations of water level for flood forecasting and river management, particularly in poorly instrumented catchments. In this study, we present an efficient calibration approach for hydraulic models based on a steady-state hydraulic solver and CryoSat-2 observations. In order to ensure that only coherent forcing/observation pairs are considered in the calibration, we first propose an outlier filtering approach for CryoSat-2 observations in data-scarce regions using simulated runoff produced by a hydrologic model. In the hydraulic calibration, a steady-state solver computes the WSE profile along the river for selected discharges corresponding to the days of CryoSat-2 overpass. In synthetic calibration experiments, the global search algorithm generally recovers the true parameter values in portions of the river where observations are available, illustrating the benefit of dense spatial sampling from geodetic altimetry. The most sensitive parameters are the bed elevations. In calibration experiments with real CryoSat-2 data, validation performance against both Sentinel-3 WSE and in-situ records is similar to previous studies, with RMSD ranging from 0.43 to 1.14 m against Sentinel-3 and 0.60 to 0.73 against in-situ WSE observations. Performance remains similar when transferring parameters to a one-dimensional hydrodynamic model. Because the approach is computationally efficient, model parameters can be inverted at high spatial resolution to fully exploit the information contained in geodetic CryoSat-2 altimetry.

1 **Hydraulic model calibration using CryoSat-2 observations in the Zambezi catchment**

2 **Cécile M. M. Kittel¹, Simbidzayi Hatchard², Jeffrey C. Neal², Karina Nielsen³, Paul D.**
3 **Bates², Peter Bauer-Gottwein¹**

4 ¹Department of Environmental Engineering, Technical University of Denmark, Kgs. Lyngby,
5 Denmark

6 ²School of Geography, University of Bristol, Bristol, United Kingdom

7 ³National Space Institute, Technical University of Denmark, Kgs. Lyngby, Denmark

8

9 Corresponding author: Cécile M. M. Kittel (ceki@env.dtu.dk)

10

11 **Key Points:**

- 12 • We use satellite altimetry observations from CryoSat-2 and a steady-state solver to
13 calibrate hydraulic model parameters
- 14 • We develop an outlier filtering method for CryoSat-2 observations in ungauged
15 catchments based on rainfall-runoff model simulations
- 16 • We integrate the altimetry observations in an efficient global calibration approach at low
17 cost compared to a 1D hydrodynamic model
18

19 **Abstract**

20 Geodetic altimeters provide unique observations of the river surface longitudinal profile due to
21 their long repeat periods and densely spaced ground tracks. This information is valuable for
22 calibrating hydraulic model parameters, and thus for producing reliable simulations of water
23 level for flood forecasting and river management, particularly in poorly instrumented
24 catchments. In this study, we present an efficient calibration approach for hydraulic models
25 based on a steady-state hydraulic solver and CryoSat-2 observations. In order to ensure that only
26 coherent forcing/observation pairs are considered in the calibration, we first propose an outlier
27 filtering approach for CryoSat-2 observations in data-scarce regions using simulated runoff
28 produced by a hydrologic model. In the hydraulic calibration, a steady-state solver computes the
29 WSE profile along the river for selected discharges corresponding to the days of CryoSat-2
30 overpass. In synthetic calibration experiments, the global search algorithm generally recovers the
31 true parameter values in portions of the river where observations are available, illustrating the
32 benefit of dense spatial sampling from geodetic altimetry. The most sensitive parameters are the
33 bed elevations. In calibration experiments with real CryoSat-2 data, validation performance
34 against both Sentinel-3 WSE and in-situ records is similar to previous studies, with RMSD
35 ranging from 0.43 to 1.14 m against Sentinel-3 and 0.60 to 0.73 against in-situ WSE
36 observations. Performance remains similar when transferring parameters to a one-dimensional
37 hydrodynamic model. Because the approach is computationally efficient, model parameters can
38 be inverted at high spatial resolution to fully exploit the information contained in geodetic
39 CryoSat-2 altimetry.

40 **1. Introduction**

41 Climate change and human activities have altered river regimes globally, posing significant challenges for water
42 resources managers (Mahé et al., 2013). Flood and drought patterns are changing calling for robust flood hazard and
43 risk assessment. Many river basins are currently ungauged or sparsely gauged (Hannah et al., 2011), as monitoring
44 efforts and data accessibility have severely declined in recent decades (Vörösmarty et al., 2001). However, a
45 reasonable hydraulic representation of river channels is key to producing meaningful large-scale flood models and
46 typically relies on ground monitoring. Simulating river hydraulics at large scale in poorly instrumented regions
47 requires adapted model structures and simplifications to compensate for constraints on computational resources and
48 insufficient ground observations.

49 Remote sensing observations can be used to retrieve hydraulic parameters and have become a key supplement to in-
50 situ observations in hydrological studies. When parameters cannot be sensed even remotely, calibration is an
51 important step to ensure that the simulated quantities agree with observations of the system (Michailovsky et al.,
52 2012). Very often, bathymetry and channel roughness need to be estimated through calibration or assumptions made
53 by the modeler, e.g. regarding channel geometry (Alsdorf et al., 2007). Effective estimation methods in data-poor
54 regions are needed.

55 Satellite radar altimeters can measure the water surface elevation (WSE) of inland water bodies, which can be used
56 as an alternative to in-situ level observations. WSE from satellite radar altimetry has been used increasingly in
57 hydrodynamic model calibration studies as a supplement to in-situ gauge data (Paiva et al., 2013; Schneider,
58 Tarpanelli, et al., 2018) or even as a possible surrogate in ungauged basins (Getirana et al., 2013; Jiang et al., 2019;
59 Liu et al., 2015). Dense water level profiles have been proven useful in the estimation of distributed hydraulic
60 parameters (F. O’Loughlin et al., 2013; Paris et al., 2016; Schumann et al., 2010). To capture the small-scale
61 variability of river morphology, the spatial sampling must be denser than what can be achieved with short-repeat
62 missions (down to 52 km at the Equator for the two Sentinel-3 satellites). In that respect, geodetic altimeters such as
63 CryoSat-2 provide the opportunity to extract longitudinal profiles of rivers.

64 Although not designed for hydrological applications, the benefit of high spatial sampling density of geodetic
65 missions for hydraulic studies has been proven in recent years (Jiang et al., 2019; Schneider, Ridler, et al., 2018;
66 Schneider, Tarpanelli, et al., 2018; Tourian et al., 2016). Schneider et al. (2018) exploited the dense spatial sampling
67 of CryoSat-2 to calibrate channel roughness in the well-gauged Po River at a finer spatial resolution. They compared

68 homogenous roughness parameters to spatially distributed parameters with increasing the spatial resolution from
 69 subreach level to 10 km-long sections. The RMSE (Root Mean Square Error) against in-situ observations improved
 70 by up to 29 cm. They showed a strong correlation between the channel sinuosity and the spatially variable calibrated
 71 channel roughness. Jiang et al. (2019) showed that missions with high spatial coverage, such as CryoSat-2,
 72 improved the RMSE against ground observations by up to 4 cm compared to missions with wider ground track
 73 spacing (i.e. the spacing between satellite tracks) such as Envisat or Jason-2 and 3. Furthermore, the sharpness of the
 74 parameter estimates increased with decreasing ground-track spacing and increasing spatial detail. Tourian et al.
 75 (2016) reached a similar conclusion in a study on spatiotemporal densification of altimetry over rivers. The quality
 76 of time series at virtual stations deteriorated slightly when including CryoSat-2 data due to assumptions pertaining to
 77 the spatial interpolation. However, CryoSat-2 decreased the bias by increasing the spatial representation of the river
 78 profile.

79 An important step in using satellite altimetry for inland water applications is outlier filtering. Typically, outliers are
 80 removed using secondary datasets such as a Digital Elevation Model (DEM) or binary water/land masks (Jiang et
 81 al., 2017; Schneider et al., 2017; Schwatke et al., 2015) or by evaluating the observations themselves, e.g. the return
 82 waveforms or the backscatter coefficients (e.g. Boergens et al., 2017; Dinardo et al., 2018; Schwatke et al., 2015;
 83 Zhang et al., 2020). For larger water bodies or short return missions, statistical outlier removal can be used to further
 84 refine the filtering (e.g. Nielsen et al., 2015; Schwatke et al., 2015; Zhang et al., 2020). For medium-sized rivers, the
 85 number of observations per ground track may be too low to perform meaningful statistical outlier removal. When
 86 bathymetry is unknown, WSE is dominated by the unknown bed elevation and errors larger than 1 m may be
 87 difficult to detect. This poses a challenge particularly for geodetic missions such as CryoSat-2, where the seasonal
 88 signal cannot be removed due to the long revisit time. The dense spatial sampling pattern is impractical for on-
 89 ground validation and comparison to traditional gauging stations would require aggregation of the observations at
 90 the expense of the valuable spatial resolution to obtain time series. Therefore, robust outlier removal procedures are
 91 needed to extract useful observations from geodetic altimetry datasets.

92 Water levels alone can only provide limited information, and the modelling and calibration problems must be
 93 adequately formulated to reflect the available observations. Getirana et al. (2013) and Liu et al. (2015) achieve good
 94 simulation results when calibrating channel roughness and bed elevation parameters simultaneously in spite of
 95 model equifinality. Jiang et al. (2019) investigated the information contained in altimetry WSE and the capability to
 96 recover parameter values (bed elevation, channel roughness and channel geometry) through calibration. Only the
 97 bed elevation could be consistently retrieved in combination with one of the other parameters. To avoid ambiguity,
 98 channel geometry can be inferred e.g. by assuming rectangular river cross-sections (Biancamaria et al., 2009; Jiang
 99 et al., 2019) or power channel shapes (Neal et al., 2015) and information from satellite imagery and global
 100 databases.

101 The inverse problem to determine hydrodynamic model parameters is highly non-linear and non-convex. Studies
 102 have used local iterative search algorithms such as Levenberg-Marquardt (Jiang et al., 2019; Schneider, Tarpanelli,
 103 et al., 2018) or global search algorithms (Getirana et al., 2013; Liu et al., 2015) to identify the optimal parameters.
 104 Global search algorithms are less sensitive to the starting point for non-convex problems; however, a higher number
 105 of simulations are usually required to search the parameter space adequately. The computational requirements to
 106 calibrate spatially distributed hydraulic parameters increase with the number of estimated parameters. Furthermore,
 107 solving the shallow water equations – even with efficient solvers – still requires long simulation time, including
 108 warm-up periods (Neal et al., 2012). Using a hydrodynamic solver in the inverse problem combined with a global
 109 search algorithm is infeasible due to resource requirements. Therefore, efficient calibration approaches balancing
 110 parameter accuracy and resources requirements are greatly needed.

111 In this study, we evaluate the combination of a steady-state solver of the shallow water equations and a global search
 112 algorithm for efficient calibration of hydraulic parameters against robustly selected CryoSat-2 observations.

113 Specifically, we

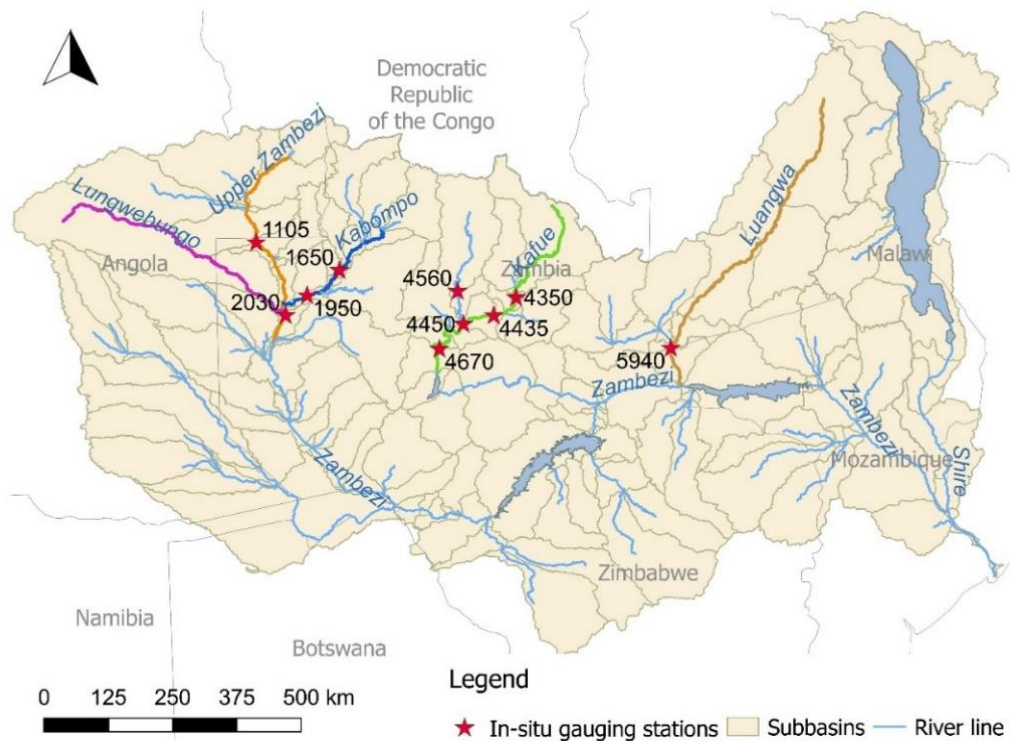
- 114 • Propose an outlier filtering method for CryoSat-2 observations suited for data-scarce regions based on
 115 runoff simulations
- 116 • Evaluate the capability of retrieving spatially distributed parameter values (i.e., channel roughness and bed
 117 elevation at least every 20 km) using a steady-state solution of the Saint-Venant equations and CryoSat-2
 118 sampling pattern in synthetic calibration experiments
- 119 • Evaluate the method using real-world CryoSat-2 observations
- 120 • Assess the performance of the calibrated parameters in dynamic state using a hydrodynamic solver

121 The proposed method is most valuable in ungauged catchments, where observations of the targeted calibrated
 122 parameters are unavailable. Synthetic experiments allow us to evaluate how the calibration performs and to identify

123 potential limitations (e.g., parameter interactions, behavioral parameters). The full workflow is then assessed for
 124 tributaries of the Zambezi, by comparing Sentinel-3 water level and in-situ gauge data with the water levels
 125 simulated using a 1D hydrodynamic model parameterized with the calibrated parameters.

126 2. Study area

127 The Zambezi is located in Southern Africa and is the fourth largest river in Africa. It is 2,574 km long and drains a
 128 1.4 million km² basin. Precipitation follows a declining North-to-South gradient, with an average of 1,500 mm in the
 129 North and 500 mm in the South. The wet season is between October and March. Flow is driven largely by the
 130 precipitation climatology but also by retention in large swamps and floodplains, and artificial reservoirs in the basin.
 131 The Zambezi provides key ecosystem services, supporting large populations of fauna and flora, but is also an
 132 important resource for the people living in the basin. We select three regions within the Zambezi as study areas: the
 133 Kafue, the Luangwa and the Upper Zambezi, upstream of the Barotse floodplain, specifically the tributaries
 134 Kabompo and Lungwebungo (**Figure 1**).
 135



136
 137 **Figure 1** Study area and in-situ gauging stations. Calibration is performed for the five
 138 highlighted reaches (Lungwebungo, Kabompo, Upper Zambezi, Kafue and Luangwa).

139 3. Data

140 3.1. Radar Altimetry

141 3.1.1. CryoSat-2

142 CryoSat-2 Level 2 data were provided by the National Space Institute, Technical University of Denmark (DTU
 143 Space) for the period 16-07-2010 to 21-03-2018. The data is based on the 20Hz Level-1b ESA dataset and has been
 144 retracked at DTU Space using an empirical retracker based on a sub-waveform threshold (Villadsen et al., 2016). In

145 the Zambezi, CryoSat-2 operates only in Low Resolution Mode (LRM). The DEM and CryoSat-2 observations are
146 reprojected onto the EGM2008 using VDatum (Myers et al., 2007).

147 3.1.2. Sentinel-3

148 The Sentinel-3 dataset is independent of the data used to calibrate the steady-state model and its virtual stations'
149 monitoring network is denser and with more recent observations than the ground network. Sentinel-3 Level-2 WSE
150 observations were obtained from the ESA GPOD (Grid Processing on Demand SAR Versatile Altimetric Toolkit for
151 Ocean Research and Exploitation) service (available on <https://gpod.eo.esa.int/>). The data has been described and
152 evaluated in Kittel et al. (2020b). Performance was quantified in the Upper Zambezi with RMSD varying between
153 2.9 and 31.3 cm. In the rest of the river catchment, there was good coherence between historical seasonal trends and
154 the Sentinel-3 water surface elevation.

155 3.2. In-situ observations

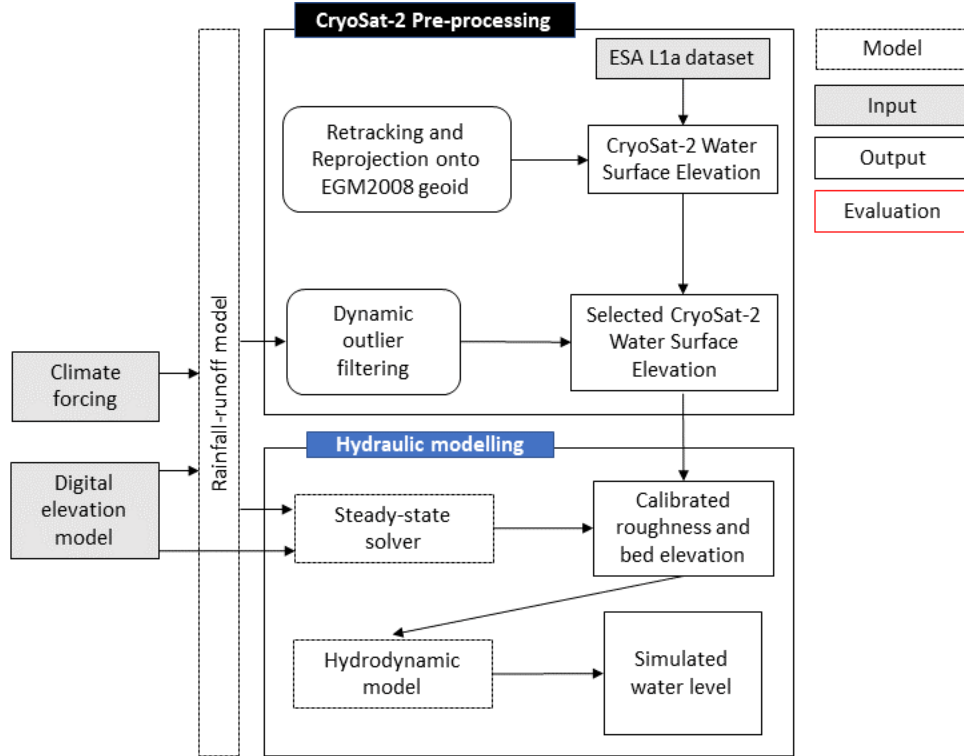
156 In situ observations were available for five subcatchments in the Upper Zambezi and in the Kafue, and two out of 12
157 subcatchments in the Luangwa (Table S1 and Figure S1). The Zambezi River Authority (ZRA) kindly provided in-
158 situ observations in the Upper Zambezi, completing the dataset from Michailovsky & Bauer-Gottwein (2014). In-
159 situ discharge was used for the calibration of the rainfall-runoff model, while in-situ stage at two stations (Kabompo
160 and Chavuma) was used to validate the hydraulic model. To avoid bias related to the vertical datum of the datasets,
161 all records are referenced to their long-term mean and only amplitudes are compared.

162 3.1. Ancillary datasets

163 The river network is delineated using TauDEM v. 5 (Tarboton, 2015) and the MERIT DEM (Multi-Error-Removed
164 Improved-Terrain Digital Elevation Model, Yamakazi et al., 2017). The model is forced using remote sensing
165 observations: GPM (Global Precipitation Model) precipitation (Huffman et al., 2014) and ECMWF ERA-Interim
166 (European Centre for Medium range Weather Forecasts - Interim Reanalysis) (Berrisford et al., 2011) temperature
167 observations for the period 2001 to August 2019.

168 4. Methods

169 The entire workflow starting from data selection and ending with hydrodynamic simulation of water levels is shown
170 in **Figure 2**. The methodology uses remote sensing inputs and two different models: a rainfall-runoff model and a
171 hydraulic model in steady-state and dynamic mode.



172
173 **Figure 2** Schematic diagram presenting an overview of the main inputs, models and outputs of the calibration
174 workflow presented in this study

175 4.1. CryoSat-2 pre-processing

176
177 First, we use the water occurrence maps from Pekel et al., (2016) to extract observations over the river. We use a
178 threshold of 10% water occurrence frequency, and allow a 90-m buffer zone around the river mask based on the
179 results from Schneider et al., (2018). The footprint in LRM is several km wide (2.5 km² with a diameter of 1.64 km)
180 and a return signal from the water surface can be captured before and after the satellite has crossed the river.
181 Parabolic distortions of the water levels due to this so-called “hooking effect” (Frappart et al., 2006; Maillard et al.,
182 2015), are expected to be negligible at the scale of the buffer applied.

183 Second, we remove observations deviating from the local value of the MERIT DEM by more than 30 m. This
184 ensures that the surface elevation is indeed within the 60 m satellite reception window. In total, CryoSat-2 crossed
185 the Zambezi basin 3,724 times during the observation period, resulting in 291,287 observations over water bodies in
186 the basin. Of those, 38,697 observations are over the river network itself. The rejection rate in step one is 10.5%,
187 yielding 34,647 observations after this step.

188 Unlike previous studies, the third step takes into account the river dynamics by using the output of the rainfall-runoff
189 model. We fit a one-dimensional smoothing spline in the space domain to the CryoSat-2 observations on each river
190 reach. The spline curve is assumed to represent the mean water level for the days of observation. The expected
191 deviation, Δy , from the mean level, y_{mean} , associated with the simulated discharge, Q , at the time of sensing
192 assuming uniform flow and a wide rectangular channel is estimated using Manning’s equation for a wide rectangular
193 channel

$$Q = \frac{1}{n} \sqrt{S} y^{\frac{5}{3}} \quad (1)$$

194 Q is the river discharge (m³/s) S is the bed slope (m/m), n is the channel roughness and y is the channel depth. Eq. 1
195 can be written for the mean discharge and water level and for the specific conditions on the day of CryoSat-2
196 overpass. By taking the log-transform and subtracting the two, we can isolate the Δy

$$\log(Q) - \log(Q_{mean}) = \frac{5}{3} (\log(y) - \log(y_{mean})) \quad (2)$$

$$\log(y) - \log(y_{mean}) = \log\left(\frac{y_{mean} + \Delta y}{y_{mean}}\right) = \frac{3}{5} \log\left(\frac{Q}{Q_{mean}}\right) \quad (3)$$

$$\Delta y = \left(\left(\frac{Q}{Q_{mean}} \right)^{\frac{3}{5}} - 1 \right) y_{mean} \quad (4)$$

197 We calculate the mean discharge, Q_{mean} , using only the days with CryoSat-2 observations. We use error
 198 propagation to estimate the total uncertainty of Δy based on assumed uncertainties of the discharge estimate, width,
 199 slope and Manning's number (**Table 1**). The effect of the spline function smoothing factor on the magnitude of the
 200 level deviation from the mean is mitigated by using an ensemble of spline curves using varying smoothing factors
 201 (0.01-4 times the number of observations in the reach). From the ensemble, we obtain different estimates of the
 202 deviation from the mean water level (Δy) for each CryoSat-2 observation. If the deviation falls outside of the
 203 predicted confidence interval of Δy for all smoothing factors the observation is rejected.
 204

205 **Table 1** Assumed uncertainties of parameters used to estimate the confidence interval of the
 206 WSE deviation Δy

Parameter	Estimate	Error propagation
Q	Daily discharge from rainfall-runoff model	+/- 25 %
Slope	From univariate spline function (minimum fixed at 10^{-5})	2 x standard deviation over the reach
Manning's n	0.035	Calibration range: 0.02-0.05
Width	GRWD database	+/- 25 %

207 4.2. Hydraulic model

208 4.2.1. Steady-state solver

209 The steady-state solver is based on the Saint-Venant equations, which express the mass balance and momentum
 210 balance equations for gradually varied one-dimensional flow in an open channel. The equations for the steady-state
 211 solver are detailed in the supporting information text, S1.
 212 Equation 4 is the general form of the equation to solve, when assuming steady flow (i.e., constant discharge over
 213 time) and lateral inflow in a rectangular channel, where RHS (Right Hand Side) is the collection of terms not
 214 containing the derivative of the depth with respect to the chainage

$$\frac{dh}{dx} = \frac{\left(\frac{Q^2}{gA^3} \frac{\partial A}{\partial x} + S_0 - \frac{Q^2}{K^2} + \frac{2Q \times q}{gA^2} \right)}{\left(1 - \frac{Q^2}{gA^3} \frac{\partial A}{\partial h} \right)}$$

$$\frac{dh}{dx} = RHS(x, h(x)) \quad (4)$$

215 Where q is the lateral inflow at chainage x . Lateral inflow consists of runoff generated by the rainfall-runoff model
 216 in tributary subcatchments, which enters the hydrodynamic model at the most upstream node, and runoff produced
 217 in the subcatchment itself, which is distributed along the chainage proportionally to the contributing area.
 218 The solver is initialized by calculating the downstream water level boundary condition using Manning's equation
 219 and a downstream slope of $2e^{-4}$ m/m at chainage, i . The downstream slope condition was chosen based on the
 220 average slope in the catchment and only affects the most downstream cross-section. The level is then calculated
 221 stepwise at Δx spatial increments, moving upstream along the channel and solving Eq. 4 either implicitly (Eq. 5)
 222 or explicitly (Eq. 6):

$$h_{i-1} = h_i - \frac{1}{2} \times (RHS(x_i, h_i) + RHS(x_{i-1}, h_{i-1})) \times \Delta x \quad (5)$$

$$h_{i-1} = h_i - RHS(x_i, h_i) \times \Delta x \quad (6)$$

223 The explicit solution is faster but requires smaller steps Δx to be stable, while the implicit solution is less sensitive to
224 the spatial increments but requires the solution of a non-linear implicit equation for h_{i-1} at each time step. We tested
225 the speed of the two solvers using a hypothetical formulation of the Kabompo reach channel. The solutions are
226 virtually identical when solving the equations for steps of less than 500 m. The implicit solver runs in 5.3 seconds,
227 whereas the explicit solution needs 0.06 seconds. Even when applying the implicit solution only to cross-sections
228 with observations, the fastest computational time remains slower (0.17 seconds), and the large spatial increments
229 affect the final solution. We therefore use the explicit solver using 250 m spatial steps. If the solution becomes
230 numerically unstable, the spatial step is subdivided into 1 m increments.
231 We define calibration cross-sections every 20 km and at each CryoSat-2 observation. Although the steady-state
232 solver is less computationally demanding than a full hydrodynamic calibration, the number of model parameters
233 must still be constrained. Because of the CryoSat-2 orbit configuration, some observations and thus cross-sections
234 are very closely spaced. This increases the number of calibration parameters and the risk of parameter correlation.
235 We therefore remove cross-sections less than 5 km apart for shorter reaches (Kabompo and Upper Zambezi) and 10
236 km apart for longer reaches (Lungwebungo, Kafue and Luangwa).

237 4.2.2. Hydrodynamic model

238 LISFLOOD-FP is a coupled 1D/2D hydrodynamic model simulating the propagation of flood waves along channels
239 (in 1D) and over floodplains (in 2D). LISFLOOD-FP has three solvers available for calculating channel flow. The
240 kinematic wave routing model only considers the friction slope, assuming that local and convective acceleration
241 terms are negligible and that the free surface gradient is equal to the bed slope. The diffusive wave model includes
242 an additional pressure term. The sub-grid channel solves the full shallow water equations with the exception of the
243 convective acceleration term (J. Neal et al., 2012). All three formulations are numerically stable (De Almeida et al.,
244 2012). The model is specifically designed for poorly gauged catchments and has been implemented for a number of
245 sites including the Niger River (J. Neal et al., 2012), the Congo (F. E. O'Loughlin et al., 2020), and rivers in the UK
246 (Sosa et al., 2020).

247 We use LISFLOOD-FP to simulate the channel hydrodynamics in the transient state. The model requires
248 information about channel geometry in the form of channel slope, channel width and bankfull depth from a DEM or
249 surveyed cross-sections. The bank elevation is derived from the MERIT DEM, the width from the GRWD database
250 and the bed elevation and channel roughness from the calibrated steady-state solver. The bankfull depth is the
251 difference between the bed and bank elevations. The resolution of the input files is 900 m instead of the 250 m used
252 by the steady-state solver to ensure reasonable computation time. The model is forced with daily discharge from
253 headwater catchments and lateral inflow, both simulated by the rainfall-runoff model. Runoff increments are
254 distributed according to the contributing area to each channel pixel, obtained from the river delineation. The model
255 is run in 1D as a means to compare the steady-state solver to a transient solver by burning in the channel bed
256 elevation into the DEM.

257 4.3. Hydrologic model

258 The CryoSat-2 pre-processing and the hydraulic model require runoff estimates. In ungauged catchments, these can
259 be obtained using a hydrologic model. In this study we use a conceptual rainfall-runoff model of the Zambezi basin.
260 The rainfall-runoff model is described in Kittel et al. (2018) and is based on the work by Zhang et al. (2008) who
261 extended the Budyko framework's concept of limits to monthly and daily time steps. The model builds on a
262 representation of the water balance through demand and supply at various levels. At each time step, Fu's
263 representation of the Budyko curve (L. Zhang et al., 2008) is used to partition precipitation into catchment retention
264 and runoff, and catchment retention into evapotranspiration, groundwater recharge and root-zone storage. The model
265 is coupled to a Nash cascade of linear reservoirs simulating tributary processes.

266 The model is calibrated against in-situ discharge records from 1990-present after careful analysis to ensure
267 hydrometeorological stationarity can be assumed between the observation and simulation periods. In order to
268 parametrize ungauged subcatchments, we use the same catchment characteristics as proposed in Kittel et al. (2020):
269 the subcatchments were grouped into calibration clusters using the European Space Agency Climate Change
270 Initiative Land Cover map v.2 (ESA, 2017) and the MERIT DEM and calibrated holistically using an aggregated
271 objective function at catchment scale allowing trade-offs between parameters in nested subcatchments. The
272 regionalization and resulting calibration zones are summarized in Table S2. Performance was then evaluated based
273 on the flow duration curves using equal flow volume classes as described in Westerberg et al. (2011) and on the
274 daily discharge climatology Root Mean Square Deviation (RMSD). Additionally we use the Kling-Gupta Efficiency

275 to quantify post-calibration performance (Gupta et al., 2009). The model setup and performance are summarized in
 276 the supporting information, in Tables S1 and S2.

277 4.4. Hydraulic model calibration

278 4.4.1. Global search algorithm and performance statistics

279 The bed elevation and channel roughness are calibrated for each cross-section using the Shuffled Complex
 280 Evolution algorithm from the University of Arizona (SCEUA) developed by Duan et al., (1992) and implemented in
 281 Python using SPOTPY (Houska et al., 2015). The algorithm uses “complexes” to sample the parameter space. The
 282 complexes are groups of parameter samples, which are evolved independently and shuffled after each evolution
 283 cycle to ensure an efficient global search. The bed elevation parameters are initialized using a spline function
 284 interpolating between the CryoSat-2 WSE observations minus one meter to adjust for the water level. The bed
 285 elevation can vary between -5 m and 3 m from this initial value. The channel roughness is initialized at 0.04 and
 286 allowed to vary between 0.018 and 0.055. The calibration objective function consists of a data misfit term
 287 comparing the residuals between the CryoSat-2 WSE and the simulated WSE

$$E_i = (w_i + z_i) - WSE_{C2,i} \quad (7)$$

288 and a smoothness preference for the two parameters along the chainage

$$Sm_i = \frac{\sqrt{(p_i - p_{i-1})^2}}{f_{smooth}} \quad (8)$$

289 f_{smooth} is the smoothness preference: smaller values will give higher weight to Sm and force the solver to move
 290 towards a smoother solution with less abrupt changes in bed elevation or channel roughness, represented by p in Eq.
 291 8. The calibration objective is

$$Obj = \sqrt{\frac{1}{2N} \left(\sum_{i=1}^N E_i^2 + \sum_{i=1}^N Sm_i^2 \right)} \quad (9)$$

292 The smoothness preference must be chosen to balance a realistic water surface and allowing features from the bed
 293 and channel roughness to be simulated. The preference is set to 1, giving equal weight to the smoothness and error
 294 objectives due to the types of parameters evaluated. Thus, the difference in magnitude between the objectives are
 295 balanced while still prioritizing a good fit between data and observation.

296 We compute three additional diagnostic performance measures to evaluate the post-calibration performance of the
 297 hydraulic model: the Pearson correlation coefficient, Spearman’s rank correlation coefficient and the non-parametric
 298 Kling-Gupta Efficiency (Pool et al., 2018). The Kling-Gupta Efficiency (KGE) combines the Pearson correlation
 299 coefficient, and the biases between mean and observed mean discharge and between the simulated and observed
 300 standard deviation. In the non-parametric version, the rank correlation is used instead, and the discharge variability
 301 performance is computed using the flow duration curve. This method is less sensitive to assumptions of data
 302 linearity, data normality and outliers (Pool et al., 2018).

303 4.4.2. Synthetic experiments

304 Synthetic calibration experiments are used to evaluate the capabilities of the steady-state solver and calibration
 305 algorithm to retrieve the bed elevation and channel roughness using CryoSat-2-type observations of WSE. We
 306 generate a synthetic set of parameters (i.e., bed elevation and Manning’s n at all cross-sections) to produce synthetic
 307 CryoSat-2 observations in the Kabompo reach, i.e., a synthetic representation of the true WSE. To reflect data
 308 uncertainties, the synthetic truth is perturbed with normally distributed random noise with varying standard
 309 deviations. The resulting three experiments are:

- 310 • 3 cm standard deviation representing in-situ water level accuracy
- 311 • 20 cm standard deviation representing high accuracy for altimetry WSE

- 312 • 40 cm standard deviation representing average accuracy for altimetry WSE

313 Parameter sensitivity is evaluated by conducting an extended Fourier amplitude sensitivity test (FAST) (Saltelli et
314 al., 1999) as implemented in SPOTPY (Houska et al., 2015). We compare the total sensitivity of the bed elevation
315 and channel roughness at each cross-section to assess the spatial sensitivity of the two parameters along the river
316 chainage. Over 686.000 model runs are performed to achieve the recommended sampling of the parameter space
317 based on the number of calibration parameters in the synthetic example (Houska et al., 2015; Saltelli et al., 1999).

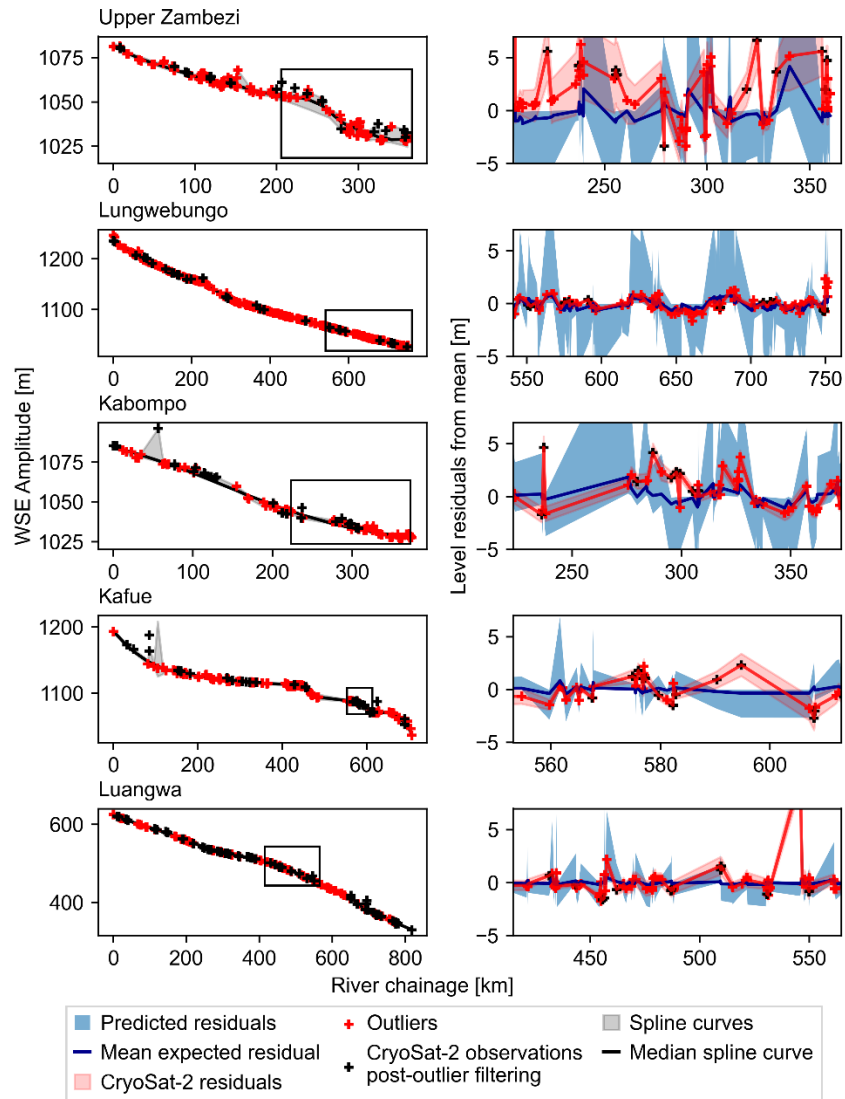
318 4.4.3. Calibration against real-world observations

319 We then use the real-world CryoSat-2 observations and calibrate the bed elevation and channel roughness in five
320 reaches in the Zambezi catchment. To ensure that the steady-state assumption is reasonable, we choose CryoSat-2
321 observations where the 10-day discharge gradient is less than 5% of the mean discharge. This is the case for 69.9%
322 of the CryoSat-2 observations. To minimize the impact of uncertainties related to the CryoSat-2 observations and
323 runoff simulations, we classify the simulated runoff and CryoSat-2 observations into discharge classes based on the
324 runoff histogram and time of observation. The steady-state model is run for each class and residuals are calculated
325 for all CryoSat-2 observations within the class.

326 5. Results

327 5.1. CryoSat-2 outliers filtering

328 **Figure 3** illustrates the CryoSat-2 river longitudinal profiles and outlier filtering for each of the five reaches. In the
329 downstream part of the Upper Zambezi, water level increases of 5 m are unlikely during the low flow season;
330 therefore, the associated CryoSat-2 observations are rejected, however a similar increase may occur during the high
331 flow season, highlighting the benefit of a dynamic threshold. The rejection rate is between 10% for Lungwebungo
332 and 24% for Luangwa.



333
 334 **Figure 3** Selection of CryoSat-2 observations in the Zambezi. Left: longitudinal profile of each
 335 studied river reach, right: illustration of the outlier filtering process for a subset of each reach.

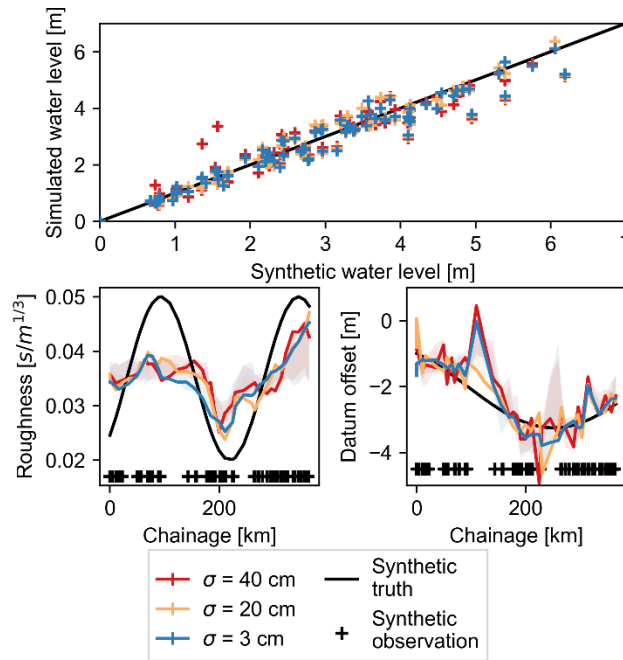
336 The main challenges in terms of outlier-filtering are adequately fitting the spline function so it is representative of
 337 the mean water surface profile along the river line. In the Upper Zambezi, Kafue and Kabompo we removed
 338 observations deviating from the spline function by more than twice the residual standard deviation and fitted a new
 339 spline function through the remaining observations, resulting in rejection rates of 18%, 19% and 23% respectively.
 340 This was necessary due to the combination of large variations in WSE and changes in the reach slope. There is a
 341 fine balance between overfitting outliers and smoothing the mean water level.

342 The Luangwa River runs from North-East to South-West. CryoSat-2 predominantly crosses the Luangwa between
 343 March and end of November, thus missing the wet season. Therefore, the CryoSat-2 observations are expected to be
 344 relatively close to the mean water elevation with very small predicted residuals. In this case the outlier filtering is
 345 particularly sensitive to the estimation of the mean water surface profile. However, reducing the smoothing factors
 346 of the spline curve ensemble also increased the risk of admitting clear outliers.

347 **5.2. Synthetic test**

348 The synthetic tests evaluate the impact of observation uncertainties by using respectively 3 cm, 20 cm and 40 cm
 349 standard deviations to perturb the synthetic CryoSat-2 observations. The results are shown in **Figure 4**.

350



351 **Figure 4** Top: Simulated against synthetic water level (the calibrated bed elevation is subtracted)
 352 for the three experiments. Bottom: Retrieval of synthetic Manning's roughness, n (left) and
 353 offset from the initial datum guess (right) by the model. The black crosses indicate the chainage
 354 of the synthetic observations consistent with the CryoSat-2 observation density.
 355

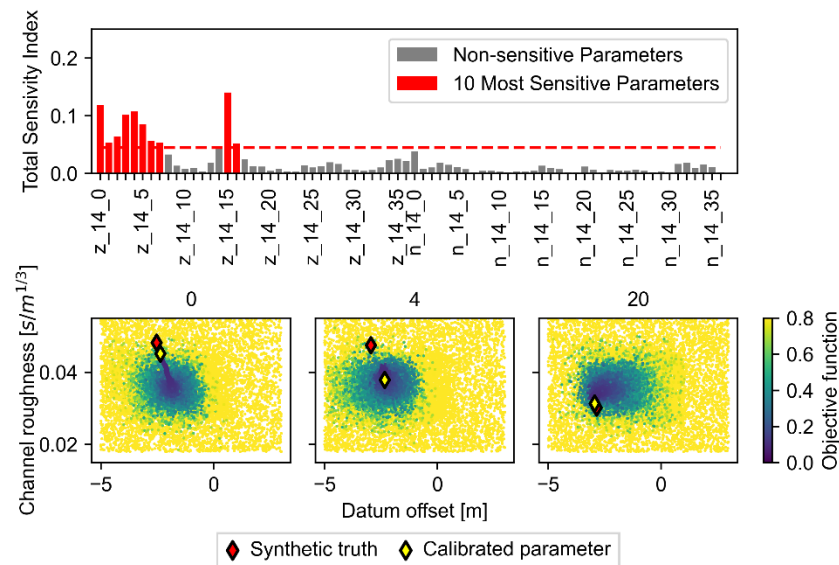
356 A difference in performance is seen when increasing the observation uncertainty, as seen in the performance
 357 statistics (**Table 2**) and the spread in the scatter plot in **Figure 4**. The RMSD is in the order of magnitude of the
 358 observation uncertainty. For all assumed uncertainty levels, parameter retrieval is most improved at cross-sections
 359 with synthetic observations. This was expected and confirms the advantage of using spatially dense observations to
 360 calibrate hydrodynamic parameters. The weighted objective used in calibration includes a smoothness factor. There
 361 is good consistency between the RMSD and calibration objective, with the smoothness factor forcing a reduction in
 362 variations where the observation density is low.

363 **Table 2** Calibration performance for the synthetic experiments at all cross-sections and at cross-
 364 sections with synthetic observations (gauged cross-sections).

Observation uncertainty	$\sigma = 40$ cm	$\sigma = 20$ cm	$\sigma = 3$ cm
WSE objective	0.26	0.15	0.09
RMSD [m]	0.33	0.17	0.08
Datum offset RMSD [m]	0.75	0.49	0.56
Considering only gauged cross-section	0.53	0.39	0.39
Manning's n RMSD [s/m ^{1/3}]	0.0083	0.0072	0.0075

365 The downstream sections are most sensitive during calibration according to the FAST sensitivity analysis. The
 366 Saint-Venant equations account for backwater effects; therefore, changes in downstream parametrization have an
 367 impact on all upstream evaluation points. Tweaking upstream parameters will mainly impact the upstream
 368 predictions in the steady-state solver and thus have limited effect on the overall performance. Sensitivity is driven by
 369 the observation density, as seen for the parameters at cross-section 12, which correspond to the first large gap in
 370 observations, and are not sensitive at all (**Figure 4** and **Figure 5**).
 371

372



373

374

375 **Figure 5** Top: FAST sensitivity analysis of the synthetic calibration test with 20 cm standard

376 deviation; the parameters are numbered from downstream to upstream cross-sections. Bottom:

377 Sampling pattern and model performance during calibration at three randomly selected cross-

378 sections. Cross-section numbering is from downstream to upstream. The objective is lowered

379 during calibration.

380 The analysis also confirms that the objective function is less sensitive to the channel roughness, n , than the datum

381 offset, z , as shown in **Figure 5** (top). The scatter plots in **Figure 5** provide information on whether trade-offs during

382 calibration can explain the low sensitivity of the channel roughness. We plot the results of the low uncertainty

383 calibration, to remove the effect of observation uncertainty on the parameter retrieval. During calibration, the

384 parameters converge to relatively narrow parameter spaces. The synthetic truth is not always within the optimum

385 range, which is due to the global objective function and trade-offs between parameters at the different cross-

386 sections. The bed elevation and channel roughness have similar local effects: overestimating the channel roughness raises the

387 water level but can be compensated by slightly decreasing the bed elevation locally. Previous studies have shown

388 that the two parameters impact the water surface differently over different characteristic spatial scales (Durand et al.,

389 2014; Wood et al., 2016). When calibrating a single, global roughness parameter, the bed elevation will tend to have

390 a local impact, whereas adjustments of the friction parameter will have a more diffuse effect and impact a longer

391 portion of the reach. Thus, the two parameters can be retrieved simultaneously. In this study, both parameters are

392 calibrated locally, and both have a local impact. This can be seen at cross-section 0, where the best performing

393 parameter samples (objective function less than 0.2) form a straight line towards the synthetic truth. Thus, although

394 parameters can be retrieved successfully at some cross-sections, there is still model ambiguity (e.g., at cross-section

395 4). The ambiguity can be partially resolved by increasing the observation density.

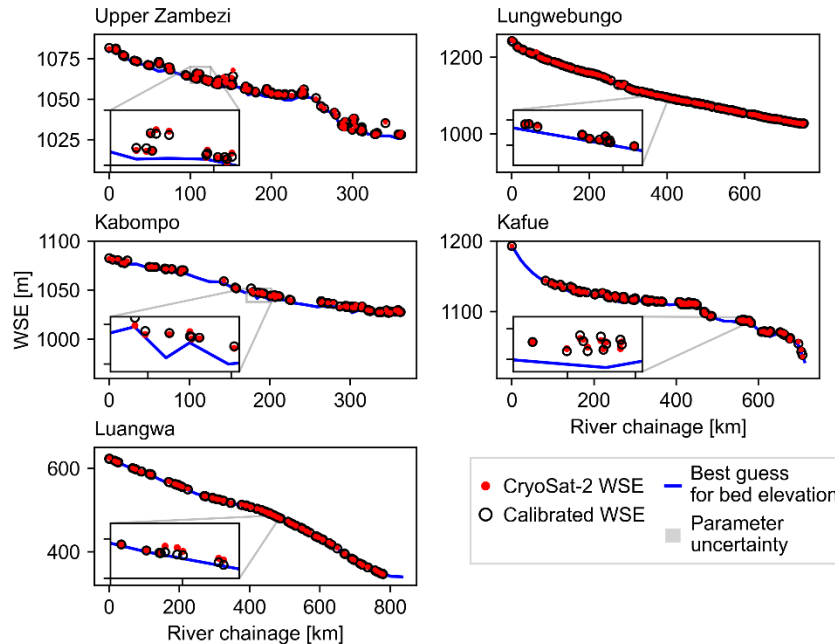
396 5.3. Calibration using real-world CryoSat-2 observations in the Zambezi

397 **Figure 6** shows the calibrated longitudinal water surface profiles at the five locations in the Zambezi after

398 calibrating the steady-state solver against real-world CryoSat-2 observations. Overall, the simulated WSE

399 corresponds quite well to the CryoSat-2 observations.

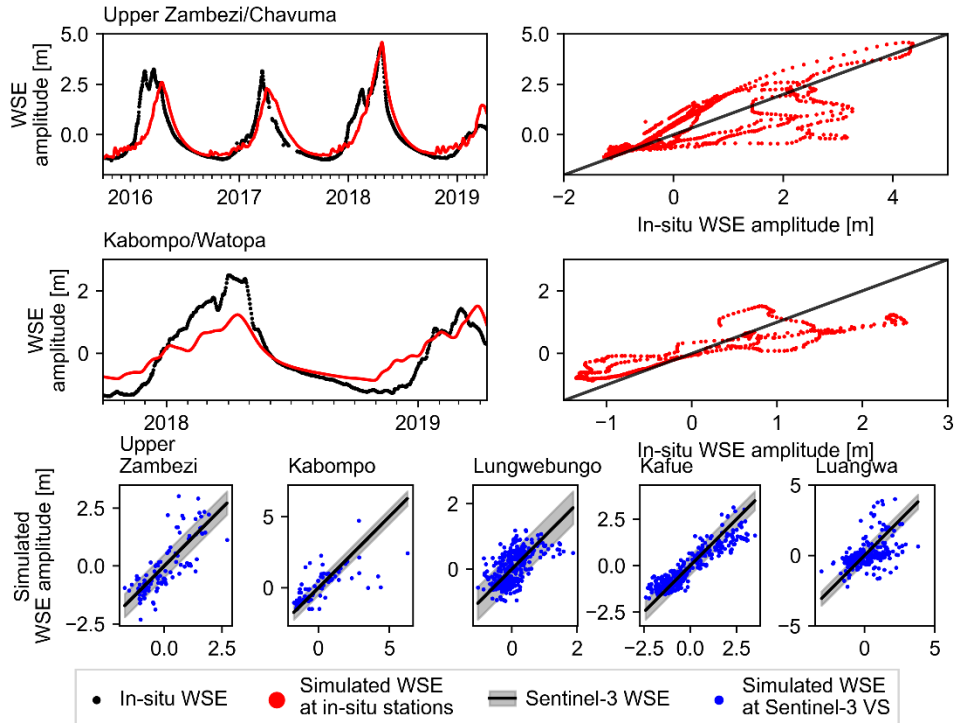
400



401 **Figure 6** Calibrated longitudinal profile of the bed elevation and the WSE simulated by the
 402 steady-state solver for the five subreaches in the Zambezi – the calibrated WSE is computed
 403 using the discharge of the corresponding day of observation by CryoSat-2 assuming steady-state.
 404

405 LISFLOOD-FP models are run for each reach using the calibrated channel roughness and bed elevation. **Table 3**
 406 summarizes performance statistics of the calibration and evaluation based on the steady-state solver and the transient
 407 solution respectively. We compare the simulated and observed water level by subtracting calibrated bed elevation
 408 from the satellite altimetry WSE. This removes the otherwise dominating effect of elevation on the performance.
 409 Overall performance is good and consistent across performance metrics. The weighted objective includes a
 410 smoothness and shallowness preference and is therefore generally larger than the RMSD. There is a good correlation
 411 between the simulated WSE and CryoSat-2 WSE. The RMSD is between 0.58 m and 0.88 m.

412 **Figure 7** shows the WSE time series simulated by LISFLOOD-FP against the in-situ records at Chavuma and
 413 Watopa and against the Sentinel-3 WSE. We note that there are some timing issues in the water level prediction,
 414 particularly at Chavuma, and in the low flow predictions at Watopa. These are consistent with uncertainties in the
 415 rainfall-runoff model, which forces the steady-state hydraulic model and hydrodynamic models. Sentinel-3 is a SAR
 416 altimeter and expected to have a lower uncertainty than a conventional altimeter (3-30 cm in the Zambezi, according
 417 to Kittel et al., 2020b). We represent the Sentinel-3 data with a slightly higher uncertainty, as the stations used in
 418 this study could not all be evaluated against in-situ observations. A conservative upper bound of 50 cm, consistent
 419 with previous studies on altimetry observations of inland water (Villadsen et al., 2016) was therefore selected to
 420 indicate the Sentinel-3 uncertainty in **Figure 7**.



421
 422 **Figure 7** Dynamic WSE at in-situ stations Chavuma (Upper Zambezi – top row) and Watopa
 423 (Kabompo – middle row) and simulated by LISFLOOD-FP and Sentinel-3 WSE versus
 424 simulated WSE by LISFLOOD-FP at Sentinel-3 VS (bottom row). The shaded area represents
 425 the expected uncertainty of Sentinel-3 of up to 50 cm.

426 The steady-state and transient solutions differ by around 20 to 40 cm in RMSD against CryoSat-2 observations,
 427 which is in the order of magnitude of the expected CryoSat-2 uncertainty in LRM (Villadsen et al., 2016). The
 428 difference between the steady-state and transient solution (22 cm to 98 cm) can be partly explained by 1) the
 429 difference between the subgrid representation of the channel and the 1-dimensional line representation of the steady-
 430 state solver and 2) the coarser spatial resolution (900 m instead of 250 m) needed to allow reasonable computation
 431 time. The performance metrics remain comparable or better than results reported in previous studies.
 432

433 **Table 3** Steady-state (SS) solver and LISFLOOD-FP (L) performance statistics using calibrated
 434 parametrization and CryoSat-2 observations (C2), Sentinel-3 (S3) WSE and in-situ water level
 435 observations. The Pearson and Spearman correlation coefficients are calculated by subtracting
 436 the calibrated bed elevation from the CryoSat-2 observations to remove the effect of elevation on
 437 the performance. A p-value below 2.5% is considered significant – in all cases the p-value is
 438 below the threshold and the correlation is significant.

	Weighted objective	RMSD					Non-parametric KGE		Pearson r^2			Spearman r^2		
		C2	S3	In-situ	C2	In-situ	C2	S3	In-situ	C2	S3	In-situ		
Data source	C2	C2	S3	In-situ	C2	In-situ	C2	S3	In-situ	C2	S3	In-situ		
Solver	SS	SS vs. L	L	L	L	L	L	L	L	L	L	L		
Upper Zambezi	0.68	0.39	0.83	0.79	0.71	0.73	0.79	0.25	0.91	0.79	0.84	0.79	0.82	0.92
Lungwebungo	0.78	0.98	0.88	1.31	0.43		0.50		0.37	0.58		0.53	0.58	

Kabompo	0.45	0.32	0.61	0.71	1.14	0.60	0.89	0.49	0.90	0.69	0.90	0.90	0.79	0.90
Kafue	0.74	0.35	0.89	1.05	0.62		0.78		0.85	0.91		0.85	0.90	
Luangwa	0.54	0.17	0.66	0.60	0.99		0.11		0.58	0.43		0.44	0.61	

439 Overall, the performance is consistent with previous studies with RMSD values between 0.60 and 1.31 m. Jiang et
 440 al. (2019) obtained RMSD between the simulated and altimetry WSE between 0.72 m and 1.6 m, when using
 441 various combinations of altimetry datasets, with CryoSat-2 alone giving a calibration performance of 1.28 m.
 442 Domeneghetti et al. (2014) obtained a RMSD of around 1 m using Envisat data to calibrate a hydrodynamic model
 443 of the Po river. O'Loughlin et al. (2020) achieved RMSD between 0.84 and 2.02 m in the Congo when comparing a
 444 large-scale hydraulic model forced with in-situ and simulated discharge. As in this study, the channel depths and
 445 friction were calibrated against satellite altimetry WSE observations; however, the study used a global channel
 446 friction parameter.
 447

448 6. Discussion

449 6.1. CryoSat-2 data selection

450 The CryoSat-2 observations used in the calibration must be accurate and representative of the river WSE. CryoSat-2
 451 is not error-free and is difficult to validate due to the high spatial sampling but low temporal sampling frequency. In
 452 this study, we used hydrological simulations from a calibrated hydrological model to assess the validity of the
 453 CryoSat-2 observations. Instead of selecting a fixed threshold to assess the deviation of a given CryoSat-2
 454 observation from the local river surface longitudinal profile, we predict the expected range of water level deviation
 455 based on the hydrological conditions in the reach at the time of observation.
 456 Robust outlier removal is essential but highly challenging in poorly instrumented catchments. By exploiting
 457 simulations of discharge, which are already available as input to the hydraulic model, a more refined method was
 458 developed in this study. Valid observations may be rejected due to errors in the corresponding simulated discharge.
 459 This is likely to occur in poorly gauged catchments, where calibration is constrained by data availability. Retaining
 460 these observations may introduce errors in the calibration, as it fits the parameters to produce water levels, which are
 461 unlikely to have occurred under the simulated flow conditions. In this study, we demonstrate the method in a
 462 sparsely gauged catchment, where the added value of altimetry WSE is high. In future studies, we recommend
 463 applying this method in a highly instrumented catchment to validate the proposed method.

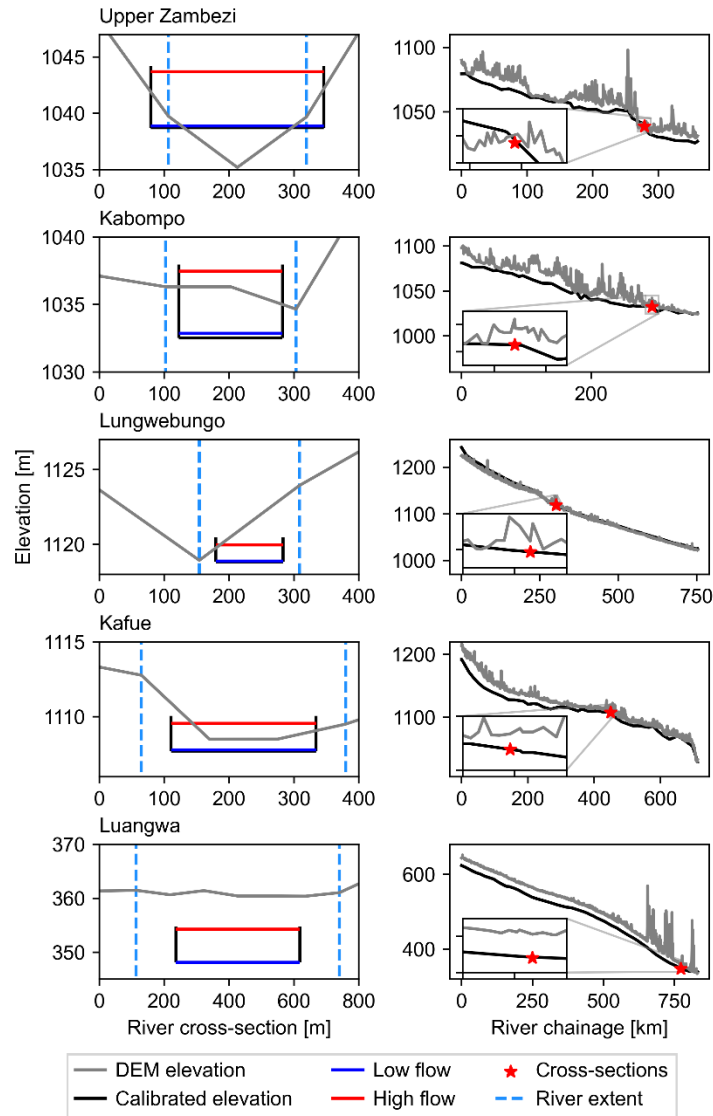
464 6.2. Model performance

465 The steady-state assumption of the solver is a simplification of the actual hydrodynamic conditions; it can be run for
 466 specific time steps corresponding to satellite overpasses greatly reducing computational time. The results are in the
 467 order of magnitude of the calibration data uncertainty and comparable to previous studies. This confirms that the
 468 method can be used to calibrate hydraulic models efficiently against spatially dense WSE observations.
 469 Furthermore, simplifications are necessary to represent poorly instrumented river channels for hydraulic modelling.
 470 In particular, some assumption on the cross-section geometry is required (e.g., trapezoidal, rectangular channel,
 471 power channel). In this study, we select a simple rectangular shape, and use global river width databases to obtain
 472 the missing information about the mean width. An alternative approach could be to use a power-law to correlate the
 473 area and water depth and the conveyance and water depth, removing the need for an explicit definition of the
 474 channel shape.
 475 Neal et al. (2015) investigated incorporating the channel cross-section uncertainty into large-scale flood inundation
 476 models of data sparse areas and showed that performance improved in models with calibrated channel friction and
 477 rectangular channels. Their results suggest that a channel shape parameter, roughness and elevation could be fitted
 478 simultaneously, provided sufficient dynamic observations are available in the reach. Neal et al. (2015) also showed
 479 that informing the model with even basic information about the channel geomorphology, such as width-discharge
 480 curves from optical or radar satellite imagery improved model calibration against level observations. The shape and
 481 friction have similar effects locally and calibrating the shape parameter may be more appropriate than calibrating
 482 friction for narrow channels, where the assumption of a rectangular shape is less appropriate.

483 The calibration of local variations in channel roughness greatly increases the parameter space, and poses a further
484 challenge. Jiang et al. (2019) demonstrated that altimetry alone is insufficient to calibrate geometry parameters as
485 well as a spatially distributed channel roughness. The reason for this is clear: local channel conveyance depends on
486 both the channel roughness and flow area. Thus, there is model ambiguity and additional datasets are required to
487 constrain the increased parameter space (e.g., channel width under known flow conditions). The unknown channel
488 bed elevation prevents a satisfactory calibration of the level to area relationship and channel roughness. Thus, an
489 interesting future path could include exploring whether the geometry parameters could be sufficiently constrained
490 from alternative or new remote sensing observations, or whether calibrating local changes in channel geometry may
491 be more robust than calibrating the channel roughness.

492 6.3. 1D versus 2D hydrodynamic model

493 The steady-state solver is one-dimensional and thus does not include bank overflow and floodplain processes. This
494 will introduce errors in shallow reaches during extreme events, where the peak water level might be over-predicted
495 to accommodate the high flow in a rectangular channel. Therefore, we only consider tributary branches of the
496 Zambezi. The subgrid solver in LISFLOOD-FP calculates the floodplain water level when the level in the channel
497 exceeds the bank elevation. This requires a robust match between bed and bank elevation. **Figure 8** illustrates the
498 calibrated cross-sections versus the DEM at selected locations of the five reaches. Because the steady-state solver
499 only calibrates the bed elevation, the bank elevation is extracted from the DEM. This poses a challenge if the
500 calibrated bed is equal to or higher than the DEM elevation height, e.g., in the Upper Zambezi (**Figure 8**). The
501 calibration information then becomes obsolete. If the difference is too small, the channel might overflow too often
502 (as might be the case at Kabompo). Thus to apply the results in a 2D modelling setup, the bank elevation must be
503 corrected, to ensure the channel is correctly burned into the floodplain, e.g. using SAR imagery to deduce the bank
504 and bed elevation relationship (Wood et al., 2016). Despite the higher demands for parametrization and computation
505 power, a two-dimensional solver would be necessary to adequately model the entire Zambezi, particularly the delta,
506 which is not included in this study. The proposed method may however still be a useful steppingstone for more
507 complex modelling efforts, particularly in poorly instrumented catchments.



508

509 **Figure 8** Selected calibrated river cross-sections versus MERIT DEM bed and bank elevations
 510 (left) and calibrated bed elevation versus the MERIT DEM river surface longitudinal profiles
 511 (right).

512 The DEM will usually give the elevation of the water surface in the channel at time of observation. This means that
 513 the calibrated bed elevation is more likely to be below than above the DEM elevation. The opposite occurs at
 514 Chavuma, where the slope is very high. CryoSat-2 observations before and after the drop in elevation force a
 515 compromise.

516 7. Conclusion

517 A reasonable hydraulic representation of river channels for large-scale flood modeling is essential but challenging to
 518 obtain in data poor regions. In this study, we propose using a steady-state solver to calibrate hydraulic parameters
 519 against geodetic altimetry observations. We propose an informed outlier rejection framework based on simulated
 520 discharge to select CryoSat-2 observations for calibration. The approach successfully removes obvious outliers,
 521 while allowing reasonably large deviations from the estimated mean level, provided there is coherence with the
 522 hydrological conditions on the day of observation. Furthermore, it ensures that only coherent forcing/observation

523 pairs are included in the calibration. The method enables filtering spatially dense WSE observations from geodetic
 524 satellite altimetry missions in data sparse regions, where traditional outlier identification methods fail.
 525 Hydraulic parameter retrieval was evaluated in synthetic experiments, focusing on the impacts of observation
 526 density and quality, and on the calibration setup. Bed elevation was retrieved with a RMSD of 42-75 cm and channel
 527 roughness with a RMSD of 0.007-0.009 s/m^{1/3}. The calibration revealed a higher sensitivity to the elevation offset
 528 compared to the roughness parameter, resulting in a poor retrieval of the upstream channel roughness. Furthermore,
 529 we noted the effect of the WSE observation density, with the most successful performance occurring in densely
 530 observed segments of the reach. Observation uncertainty affected the retrieval of parameters at ungauged cross-
 531 sections, and performance was more similar at gauged cross-sections for the three investigated data quality
 532 scenarios.
 533 By carefully selecting observations where the steady-state assumption is reasonable, five reaches of the Zambezi
 534 were calibrated with satisfactory model performance using real CryoSat-2 observations. Calibration against real-
 535 world CryoSat-2 observations was evaluated using a range of statistical diagnostics to confirm the model behavior
 536 and compared to Sentinel-3 and in-situ observations of WSE to evaluate the temporal patterns of WSE in the river
 537 channels. The method yielded at least as good performance as past studies at far reduced computational cost and the
 538 parameter transfer from the steady-state to the transient solver did not impact performance significantly.
 539 Geodetic altimetry missions clearly hold valuable information for hydrological studies, particularly in ungauged
 540 basins. However, the dense spatial sampling requires careful data selection and comes at a computational cost
 541 because, in the hydraulic inversion, WSE must be simulated at all points of observation by the hydraulic forward
 542 model. The approach presented in this study integrates the altimetry observations in a fast and efficient, global
 543 calibration approach at low cost compared to a 1D hydrodynamic model.

544 References

- 545 De Almeida, G. A. M., Bates, P., Freer, J. E., & Souvignet, M. (2012). Improving the stability of
 546 a simple formulation of the shallow water equations for 2-D flood modeling. *Water*
 547 *Resources Research*, 48(5), 1–14. <https://doi.org/10.1029/2011WR011570>
- 548 Alsdorf, D. E., Rodríguez, E., & Lettenmaier, D. P. (2007). Measuring Surface Water From
 549 Space. *Reviews of Geophysics*, 45(2006), 1–24.
 550 <https://doi.org/10.1029/2006RG000197.1>.INTRODUCTION
- 551 Berrisford, P., Dee, D. P., Poli, P., Brugge, R., Fielding, M., Fuentes, M., et al. (2011). The
 552 ERA-Interim archive Version 2.0, (1), 23. Retrieved from
 553 <https://www.ecmwf.int/node/8174>
- 554 Biancamaria, S., Bates, P. D., Boone, A., & Mognard, N. M. (2009). Large-scale coupled
 555 hydrologic and hydraulic modelling of the Ob river in Siberia. *Journal of Hydrology*,
 556 379(1–2), 136–150. <https://doi.org/10.1016/j.jhydrol.2009.09.054>
- 557 Boergens, E., Buhl, S., Dettmering, D., Klüppelberg, C., & Seitz, F. (2017). Combination of
 558 multi-mission altimetry data along the Mekong River with spatio-temporal kriging. *Journal*
 559 *of Geodesy*, 91(5), 519–534. <https://doi.org/10.1007/s00190-016-0980-z>
- 560 Boergens, E., Nielsen, K., Andersen, O. B., Dettmering, D., & Seitz, F. (2017). Water levels of
 561 the Mekong River Basin based on CryoSat-2 SAR data classification. *Hydrology and Earth*
 562 *System Sciences Discussions*, (June), 1–22. <https://doi.org/10.5194/hess-2017-217>
- 563 Dinardo, S., Fenoglio-Marc, L., Buchhaupt, C., Becker, M., Scharroo, R., Joana Fernandes, M.,
 564 & Benveniste, J. (2018). Coastal SAR and PLRM altimetry in German Bight and West
 565 Baltic Sea. *Advances in Space Research*, 62(6), 1371–1404.
 566 <https://doi.org/10.1016/j.asr.2017.12.018>
- 567 Domeneghetti, A., Tarpanelli, A., Brocca, L., Barbetta, S., Moramarco, T., Castellarin, A., &

- 568 Brath, A. (2014). The use of remote sensing-derived water surface data for hydraulic model
569 calibration. *Remote Sensing of Environment*, 149, 130–141.
570 <https://doi.org/10.1016/j.rse.2014.04.007>
- 571 Duan, Q., Sorooshian, S., & Gupta, V. (1992). Effective and Efficient Global Optimization for
572 Conceptual Rainfall-Runoff Models. *Water Resources Research*, 28(4), 1015–1031.
- 573 Durand, M., Neal, J., Rodríguez, E., Andreadis, K. M., Smith, L. C., & Yoon, Y. (2014).
574 Estimating reach-averaged discharge for the River Severn from measurements of river
575 water surface elevation and slope. *Journal of Hydrology*, 511, 92–104.
576 <https://doi.org/10.1016/j.jhydrol.2013.12.050>
- 577 ESA. (2017). *Land Cover CCI Product User Guide Version 2. Tech. Rep.* Retrieved from
578 maps.elie.ucl.ac.be/CCI/viewer/download/ESACCI-LC-Ph2-PUGv2_2.0.pdf
- 579 Frappart, F., Calmant, S., Cauhopé, M., Seyler, F., & Cazenave, A. (2006). Preliminary results of
580 ENVISAT RA-2-derived water levels validation over the Amazon basin. *Remote Sensing of*
581 *Environment*, 100(2), 252–264. <https://doi.org/10.1016/j.rse.2005.10.027>
- 582 Getirana, A. C. V, Boone, A., Yamazaki, D., & Mognard, N. (2013). Automatic parameterization
583 of a flow routing scheme driven by radar altimetry data : Evaluation in the Amazon basin.
584 *Water Resources Research*, 49(1), 614–629. <https://doi.org/10.1002/wrcr.20077>
- 585 Gupta, H. V, Kling, H., Yilmaz, K. K., & Martinez-Baquero, G. F. (2009). Decomposition of the
586 Mean Squared Error & NSE Performance Criteria: Implications for Improving Hydrological
587 Modelling. *Journal of Hydrology*, 377(1–2), 80–91.
588 <https://doi.org/10.1016/j.jhydrol.2009.08.003>
- 589 Hannah, D. M., Demuth, S., van Lanen, H. A. J., Looser, U., Prudhomme, C., Rees, G., et al.
590 (2011). Large-scale river flow archives: Importance, current status and future needs.
591 *Hydrological Processes*, 25(7), 1191–1200. <https://doi.org/10.1002/hyp.7794>
- 592 Houska, T., Kraft, P., Chamorro-Chavez, A., & Breuer, L. (2015). SPOTting model parameters
593 using a ready-made python package. *PLoS ONE*, 10(12), 1–22.
594 <https://doi.org/10.1371/journal.pone.0145180>
- 595 Huffman, G., Bolvin, D., Braithwaite, D., Hsu, K., Joyce, R., & Xie, P. (2014). Integrated Multi-
596 satellitE Retrievals for GPM (IMERG), version 4.4. *NASA's Precipitation Processing*
597 *Center*. Retrieved from <ftp://arthurhou.pps.eosdis.nasa.gov/gpmdata/>
- 598 Jiang, L., Nielsen, K., Andersen, O. B., & Bauer-Gottwein, P. (2017). CryoSat-2 radar altimetry
599 for monitoring freshwater resources of China. *Remote Sensing of Environment*,
600 200(August), 125–139. <https://doi.org/10.1016/j.rse.2017.08.015>
- 601 Jiang, L., Madsen, H., & Bauer-Gottwein, P. (2019). Simultaneous calibration of multiple
602 hydrodynamic model parameters using satellite altimetry observations of water surface
603 elevation in the Songhua River. *Remote Sensing of Environment*, 225, 229–247.
604 <https://doi.org/10.1016/j.rse.2019.03.014>
- 605 Kittel, C. M. M., Nielsen, K., Tøttrup, C., & Bauer-Gottwein, P. (2018). Informing a
606 hydrological model of the Ogooué with multi-mission remote sensing data. *Hydrology and*
607 *Earth System Sciences*, 22, 1453–1472. <https://doi.org/10.5194/hess-22-1453-2018>
- 608 Kittel, C. M. M., Jiang, L., Tøttrup, C., & Bauer-Gottwein, P. (2021). Sentinel-3 radar altimetry

- 609 for river monitoring - A catchment-scale evaluation of satellite water surface elevation from
610 Sentinel-3A and Sentinel-3B. *Hydrology and Earth System Sciences*, 25(1), 333–357.
611 <https://doi.org/10.5194/hess-25-333-2021>
- 612 Liu, G., Schwartz, F. W., Tseng, K.-H., & Shum, C. K. (2015). Discharge and water-depth
613 estimates for ungauged rivers: Combining hydrologic, hydraulic, and inverse modeling with
614 stage and water-area measurements from satellites. *Water Resources Research*, 51, 6017–
615 6035. <https://doi.org/10.1002/2015WR017200.A>
- 616 Mahé, G., Lienou, G., Descroix, L., Bamba, F., Paturel, J. E., Laraque, A., et al. (2013). The
617 rivers of Africa: Witness of climate change and human impact on the environment.
618 *Hydrological Processes*, 27(15), 2105–2114. <https://doi.org/10.1002/hyp.9813>
- 619 Maillard, P., Bercher, N., & Calmant, S. (2015). New processing approaches on the retrieval of
620 water levels in Envisat and SARAL radar altimetry over rivers: A case study of the São
621 Francisco River, Brazil. *Remote Sensing of Environment*, 156, 226–241.
622 <https://doi.org/10.1016/j.rse.2014.09.027>
- 623 Michailovsky, C. I., & Bauer-Gottwein, P. (2014). Operational reservoir inflow forecasting with
624 radar altimetry: the Zambezi case study. *Hydrol. Earth Syst. Sci.*, 18(3), 997–1007.
625 <https://doi.org/10.5194/hess-18-997-2014>
- 626 Michailovsky, C. I., McEnnis, S., Berry, P. A. M. M., Smith, R., & Bauer-Gottwein, P. (2012).
627 River monitoring from satellite radar altimetry in the Zambezi River basin. *Hydrology and*
628 *Earth System Sciences*, 16(7), 2181–2192. <https://doi.org/10.5194/hess-16-2181-2012>
- 629 Myers, E., Hess, K., Yang, Z., Xu, J., Wong, A., Doyle, D., et al. (2007). VDatum and strategies
630 for national coverage. *Oceans Conference Record (IEEE)*.
631 <https://doi.org/10.1109/OCEANS.2007.4449348>
- 632 Neal, J., Schumann, G., & Bates, P. (2012). A subgrid channel model for simulating river
633 hydraulics and floodplain inundation over large and data sparse areas. *Water Resources*
634 *Research*, 48(W11506), 1–16. <https://doi.org/10.1029/2012WR012514>
- 635 Neal, J. C., Odoni, N. A., Trigg, M. A., Freer, J. E., Garcia-Pintado, J., Mason, D. C., et al.
636 (2015). Efficient incorporation of channel cross-section geometry uncertainty into regional
637 and global scale flood inundation models. *Journal of Hydrology*, 529, 169–183.
638 <https://doi.org/10.1016/j.jhydrol.2015.07.026>
- 639 Nielsen, K., Stenseng, L., Andersen, O. B., Villadsen, H., & Knudsen, P. (2015). Validation of
640 CryoSat-2 SAR mode based lake levels. *Remote Sensing of Environment*, 171, 162–170.
641 <https://doi.org/10.1016/j.rse.2015.10.023>
- 642 O’Loughlin, F., Trigg, M. A., Schumann, G. J. P., & Bates, P. D. (2013). Hydraulic
643 characterization of the middle reach of the Congo River. *Water Resources Research*, 49(8),
644 5059–5070. <https://doi.org/10.1002/wrcr.20398>
- 645 O’Loughlin, F. E., Neal, J., Schumann, G. J. P., Beighley, E., & Bates, P. D. (2020). A
646 LISFLOOD-FP hydraulic model of the middle reach of the Congo. *Journal of Hydrology*,
647 580(September 2019), 124203. <https://doi.org/10.1016/j.jhydrol.2019.124203>
- 648 Paiva, R. C. D., Collischonn, W., Bonnet, M. P., De Gonçalves, L. G. G., Calmant, S., Getirana,
649 A., & Santos Da Silva, J. (2013). Assimilating in situ and radar altimetry data into a large-

- 650 scale hydrologic-hydrodynamic model for streamflow forecast in the Amazon. *Hydrology*
651 *and Earth System Sciences*, 17, 2929–2946. <https://doi.org/10.5194/hess-17-2929-2013>
- 652 Paris, A., Dias de Paiva, R., Santos Da Silva, J., Medeiros Moreira, D., Calmant, S., Garambois,
653 P.-A., et al. (2016). Stage-discharge rating curves based on satellite altimetry and modeled
654 discharge in the Amazon basin. *Water Resources Research*, 53, 3787–3814.
655 <https://doi.org/10.1002/2014WR016618>.Received
- 656 Pekel, J.-F., Cottam, A., Gorelick, N., & Belward, A. S. (2016). High-resolution mapping of
657 global surface water and its long-term changes. *Nature*, 540(7633), 418–422.
658 <https://doi.org/10.1038/nature20584>
- 659 Pool, S., Vis, M., & Seibert, J. (2018). Evaluating model performance: towards a non-parametric
660 variant of the Kling-Gupta efficiency. *Hydrological Sciences Journal*, 63(13–14), 1941–
661 1953. <https://doi.org/10.1080/02626667.2018.1552002>
- 662 Saltelli, A., Tarantola, S., & Chan, K. P. (1999). A Quantitative Model-Independent Method for
663 Global Sensitivity Analysis of Model Output A Quantitative Model-Independent Method
664 for Global Sensitivity Analysis of Model Output. *Technometrics*, 41(1), 39–56.
- 665 Schneider, R., Godiksen, P. N., Villadsen, H., Madsen, H., & Bauer-Gottwein, P. (2017).
666 Application of CryoSat-2 altimetry data for river analysis and modelling. *Hydrology and*
667 *Earth System Sciences*, 21, 751–764. <https://doi.org/10.5194/hess-21-751-2017>
- 668 Schneider, R., Ridler, M. E., Godiksen, P. N., Madsen, H., & Bauer-Gottwein, P. (2018). A data
669 assimilation system combining CryoSat-2 data and hydrodynamic river models. *Journal of*
670 *Hydrology*, 557, 197–210. <https://doi.org/10.1016/j.jhydrol.2017.11.052>
- 671 Schneider, R., Tarpanelli, A., Nielsen, K., Madsen, H., & Bauer-Gottwein, P. (2018). Evaluation
672 of multi-mode CryoSat-2 altimetry data over the Po River against in situ data and a
673 hydrodynamic model. *Advances in Water Resources*, 112, 17–26.
674 <https://doi.org/10.1016/j.advwatres.2017.11.027>
- 675 Schumann, G., Di Baldassarre, G., Alsdorf, D., & Bates, P. D. (2010). Near real-time flood wave
676 approximation on large rivers from space: Application to the River Po, Italy. *Water*
677 *Resources Research*, 46(5), 1–8. <https://doi.org/10.1029/2008WR007672>
- 678 Schwatke, C., Dettmering, D., Bosch, W., & Seitz, F. (2015). DAHITI - An innovative approach
679 for estimating water level time series over inland waters using multi-mission satellite
680 altimetry. *Hydrology and Earth System Sciences*, 19(10), 4345–4364.
681 <https://doi.org/10.5194/hess-19-4345-2015>
- 682 Sosa, J., Sampson, C., Smith, A., Neal, J., & Bates, P. (2020). A toolbox to quickly prepare flood
683 inundation models for LISFLOOD-FP simulations. *Environmental Modelling and Software*,
684 123(October 2019), 104561. <https://doi.org/10.1016/j.envsoft.2019.104561>
- 685 Tarboton, D. (2015). TauDEM Version 5. *Hydrology Research Group, Utah State University*.
686 Retrieved from <http://hydrology.usu.edu/taudem/taudem5/documentation.html>
- 687 Tourian, M. J., Tarpanelli, A., Elmi, O., Qin, T., Brocca, L., Moramarco, T., & Sneeuw, N.
688 (2016). Spatiotemporal densification of water level time series by multimission satellite
689 altimetry. *Water Resources Research*, 52, 613–615.
690 <https://doi.org/10.1029/2008WR006912>.M

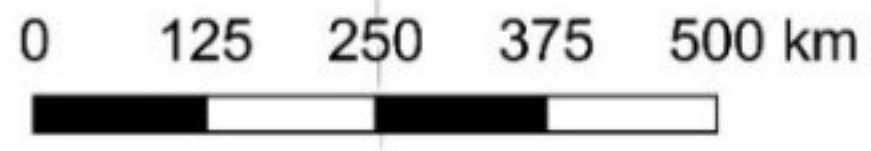
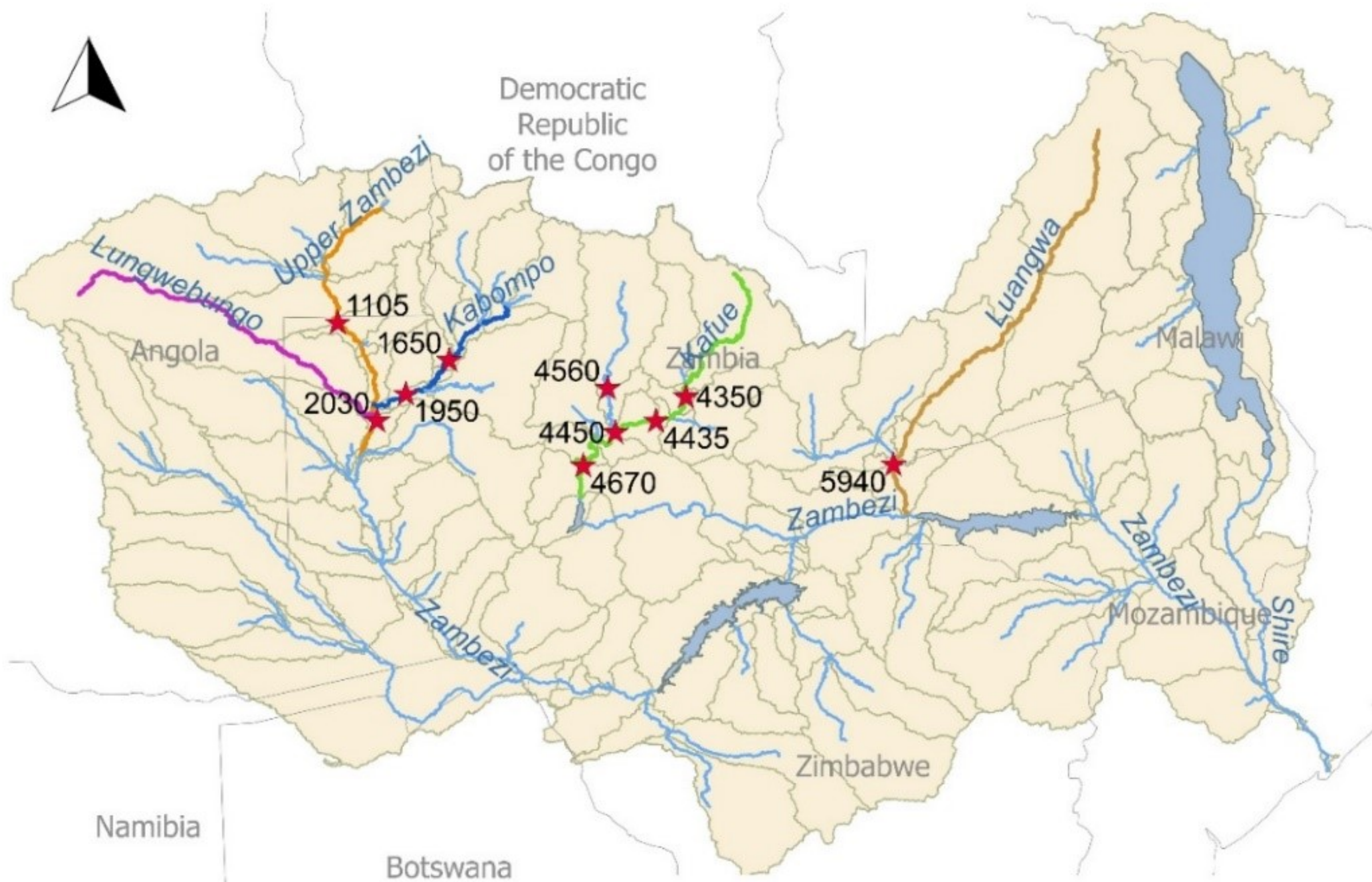
- 691 Villadsen, H., Deng, X., Andersen, O. B., Stenseng, L., Nielsen, K., & Knudsen, P. (2016).
692 Improved inland water levels from SAR altimetry using novel empirical and physical
693 retrackers. *Journal of Hydrology*, 537, 234–247.
694 <https://doi.org/10.1016/j.jhydrol.2016.03.051>
- 695 Vörösmarty, C., Askew, A., Grabs, W., Barry, R. G., Birkett, C., Döll, P., et al. (2001). Global
696 water data: A newly endangered species. *Eos*, 82(5), 54–58.
697 <https://doi.org/10.1029/01EO00031>
- 698 Westerberg, I. K., Guerrero, J. L., Younger, P. M., Beven, K. J., Seibert, J., Halldin, S., et al.
699 (2011). Calibration of hydrological models using flow-duration curves. *Hydrology and*
700 *Earth System Sciences*, 15(7), 2205–2227. <https://doi.org/10.5194/hess-15-2205-2011>
- 701 Wood, M., Hostache, R., Neal, J., Wagener, T., Giustarini, L., Chini, M., et al. (2016).
702 Calibration of channel depth and friction parameters in the LISFLOOD-FP hydraulic model
703 using medium-resolution SAR data and identifiability techniques. *Hydrology and Earth*
704 *System Sciences*, 20(12), 4983–4997. <https://doi.org/10.5194/hess-20-4983-2016>
- 705 Zhang, L., Potter, N., Hickel, K., Zhang, Y., & Shao, Q. (2008). Water balance modeling over
706 variable time scales based on the Budyko framework - Model development and testing.
707 *Journal of Hydrology*, 360, 117–131. <https://doi.org/10.1016/j.jhydrol.2008.07.021>
- 708 Zhang, X., Jiang, L., Kittel, C. M. M., & Yao, Z. (2020). On the performance of Sentinel-3
709 altimetry over new reservoirs : Approaches to determine on-board a-priori elevation.
710 *Geophysical Research Letters*, 47(17), 1–11. <https://doi.org/10.1029/2020GL088770>

711

712 **Acknowledgments, Samples and Data**

713 The authors wish to thank the Zambezi River Authority (ZRA) for kindly providing the in-situ observations in the
714 Upper Zambezi used to evaluate the WSE simulations. The data can requested from the ZRA for research purposes.
715 The Sentinel-3 data used in this study can be freely processed on and downloaded from the ESA GPOD (Grid
716 Processing on Demand SAR Versatile Altimetric Toolkit for Ocean Research and Exploitation) service (available on
717 <https://gpod.eo.esa.int/>, last accessed 14/10/2020). The MERIT DEM used as reference elevation and in the river
718 delineation was obtained from http://hydro.iis.u-tokyo.ac.jp/~yamada/MERIT_DEM/, last accessed 14/10/2020).
719 The rainfall-runoff model source code is open source and part of the GlobWetland Africa QGIS Toolbox (available
720 on <http://globwetland-africa.org/?wpdmpro=globwetland-toolbox-1-5>, last accessed 17/11/2020). LISFLOOD-FP
721 can be requested on <http://www.bristol.ac.uk/geography/research/hydrology/models/lisflood/downloads/> (last
722 accessed 17/11/2020). The CryoSat-2 observations and model parameters will be made available on Zenodo and are
723 provided as supplement to this article.

Figure 1.



Legend

- ★ In-situ gauging stations
- Subbasins
- River line

Figure 2.

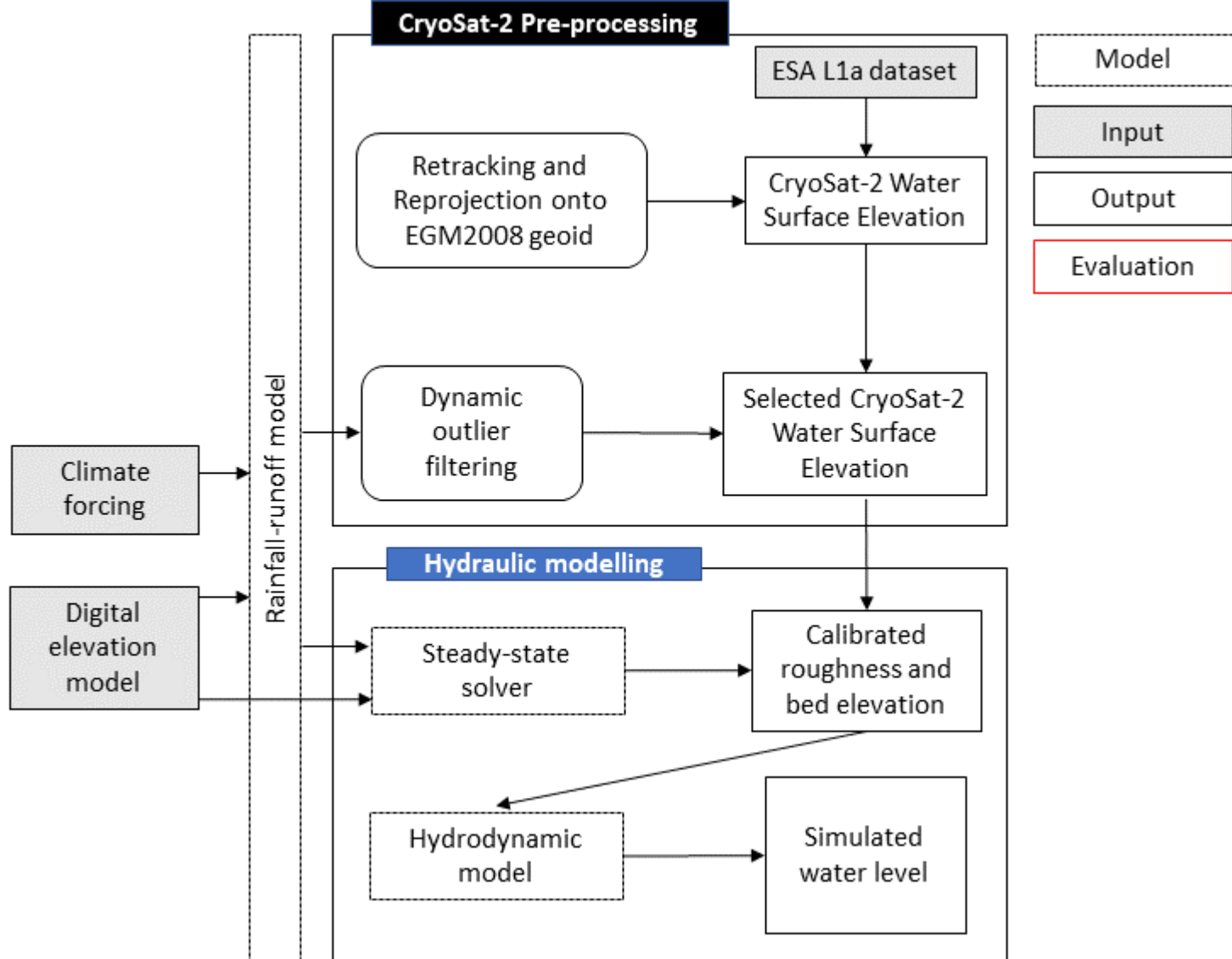


Figure 3.

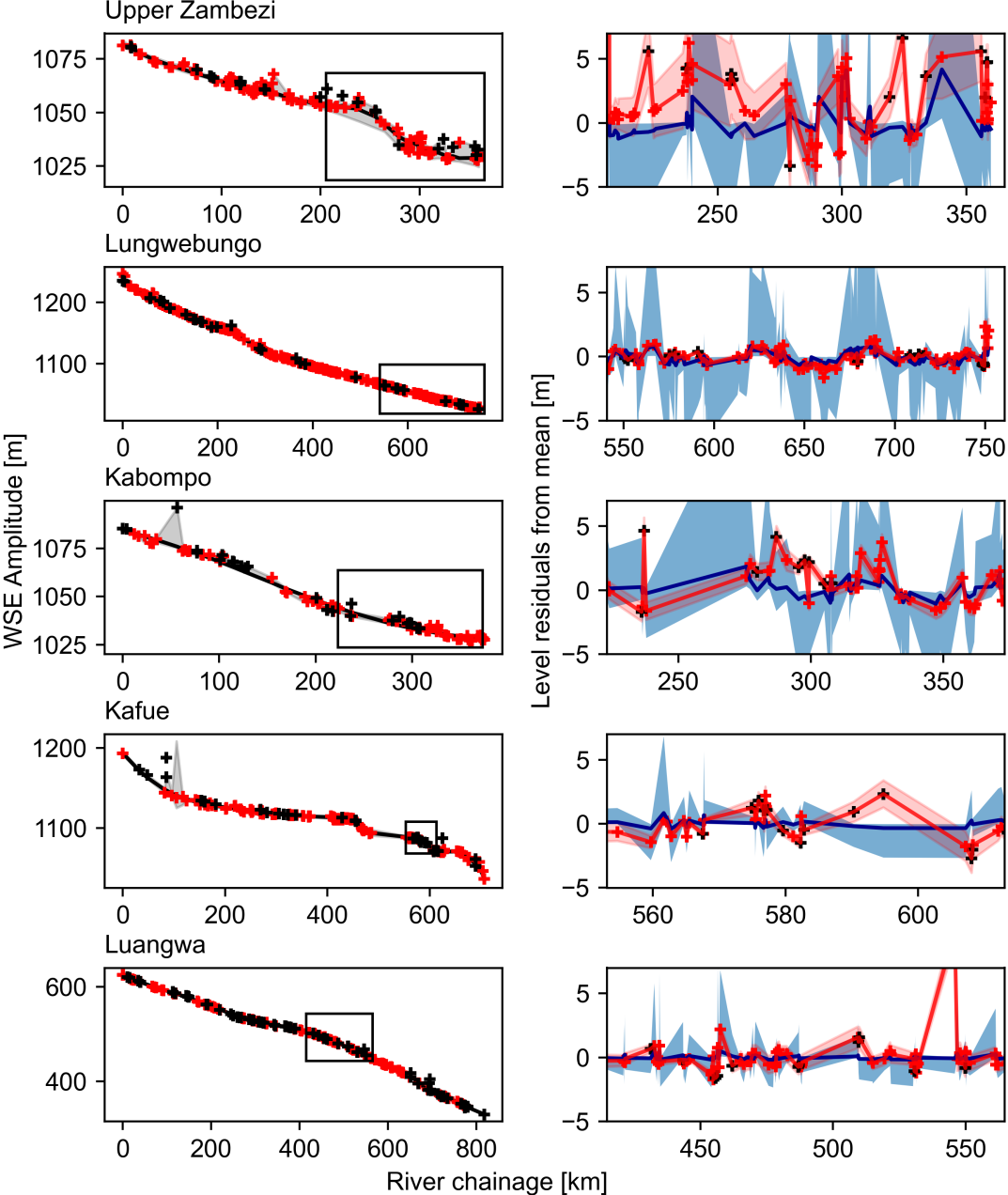


Figure 4.

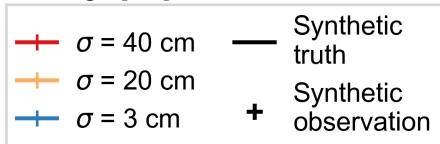
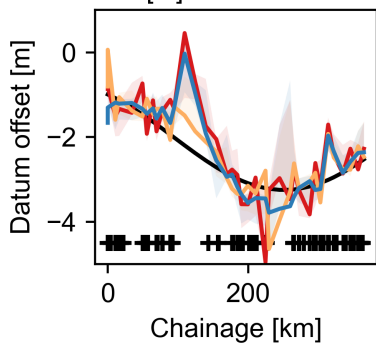
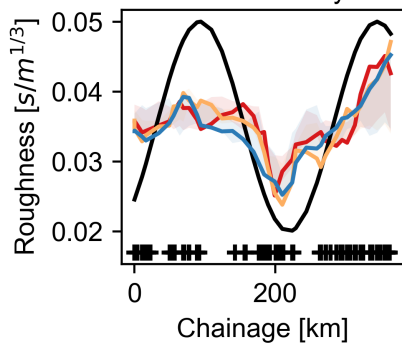
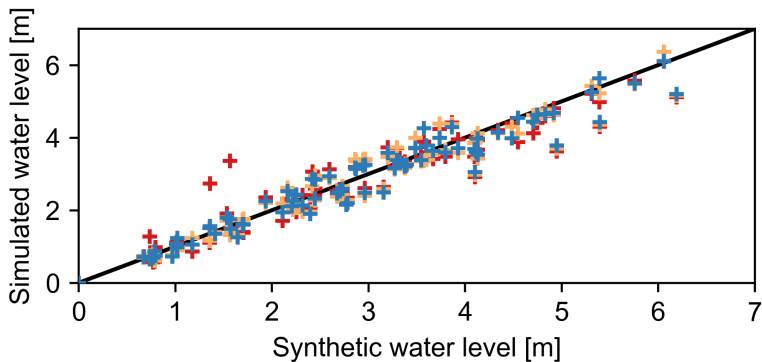


Figure 5.

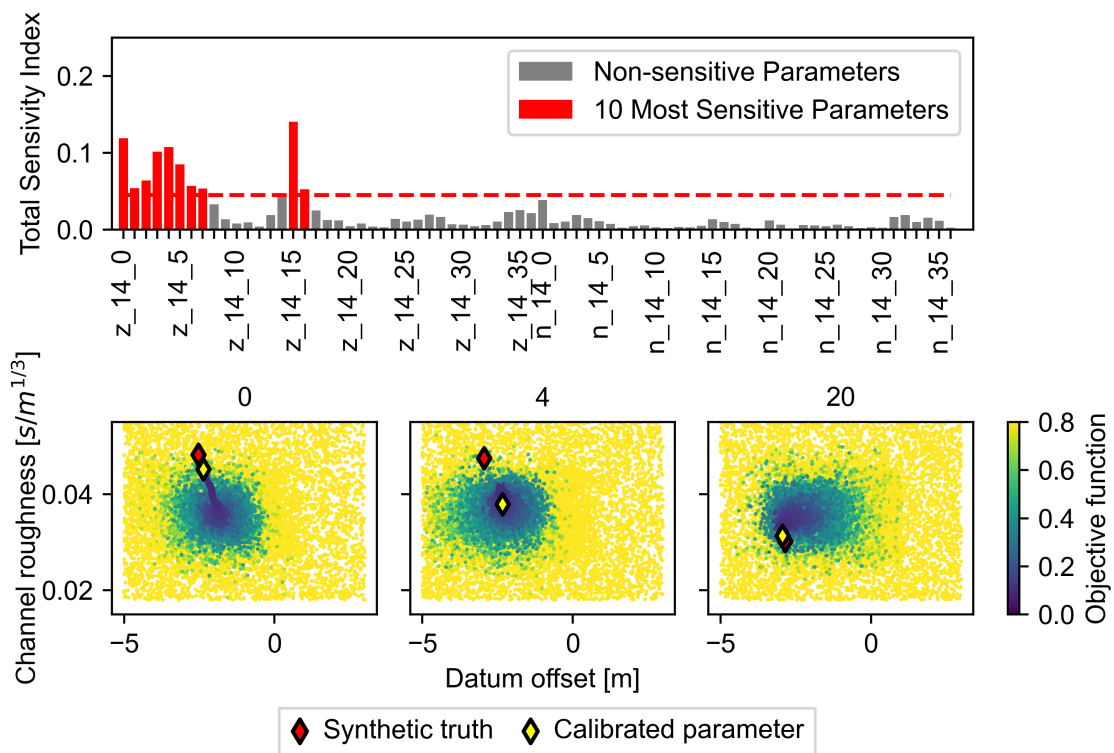
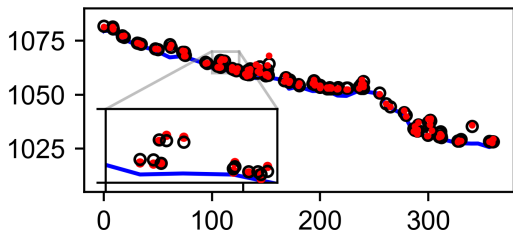
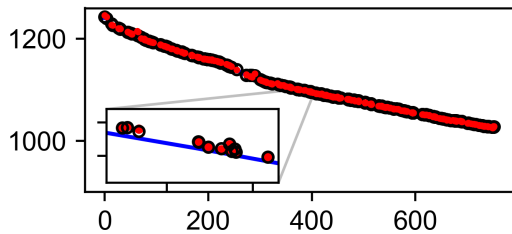


Figure 6.

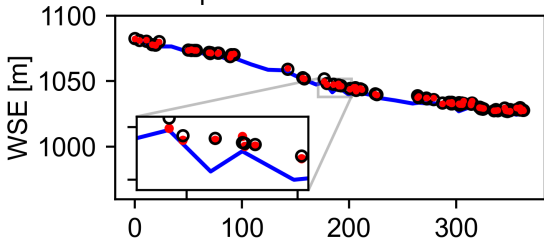
Upper Zambezi



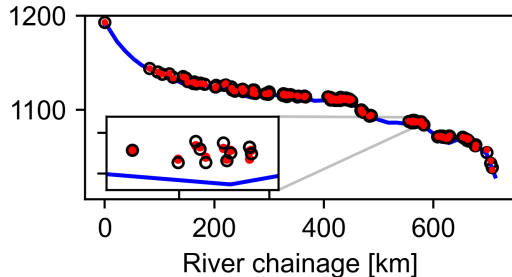
Lungwebungo



Kabompo



Kafue



Luangwa

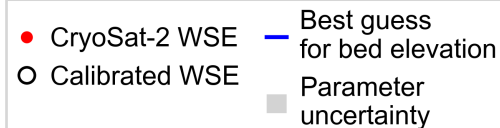
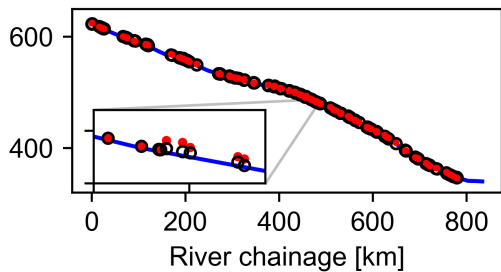
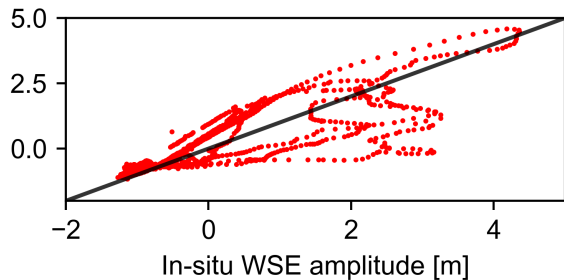
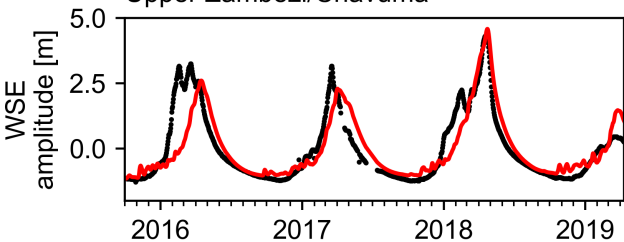
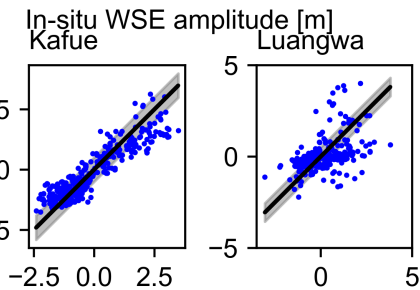
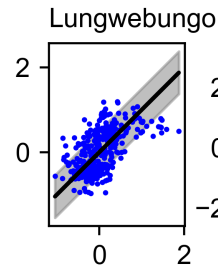
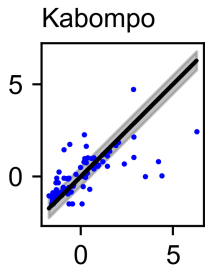
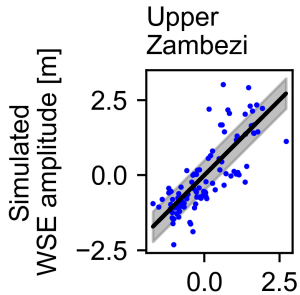
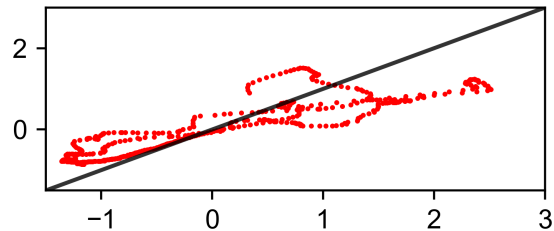
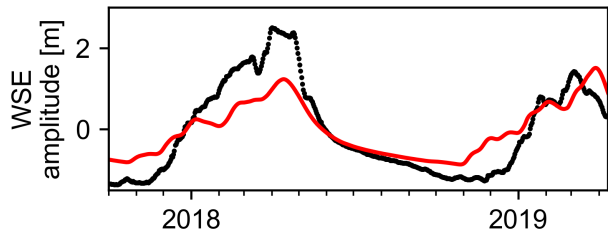


Figure 7.

Upper Zambezi/Chavuma



Kabompo/Watopa



● In-situ WSE

● Simulated WSE
at in-situ stations

— Sentinel-3 WSE

● Simulated WSE
at Sentinel-3 VS

Figure A1.

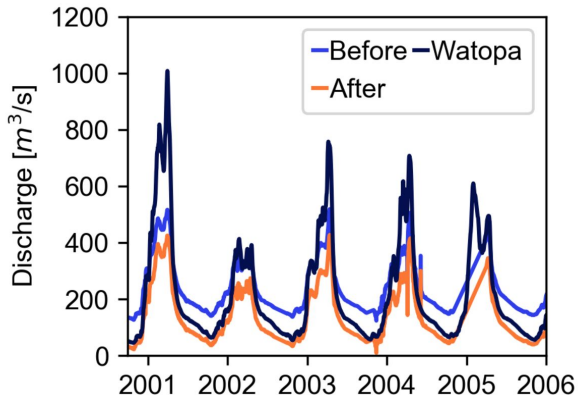
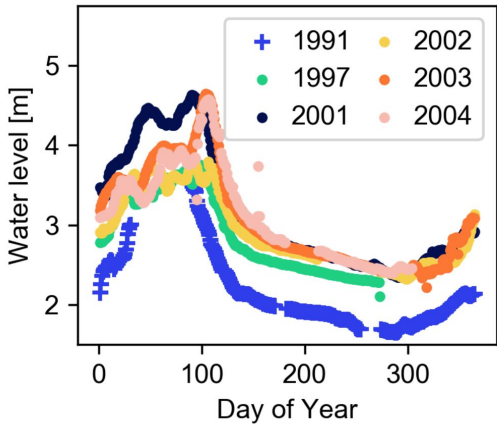
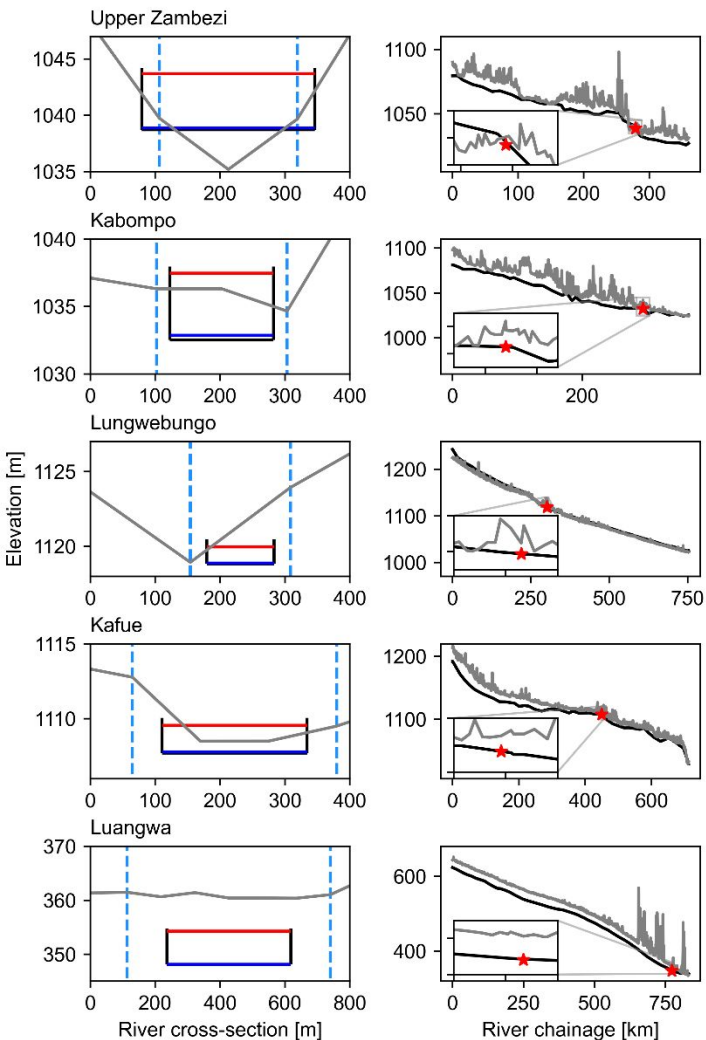


Figure 8.



Water Resources Research

Supporting Information for

Hydraulic model calibration using CryoSat-2 observations in the Zambezi catchment

Cécile M. M. Kittel¹, Simbidzayi Hatchard², Jeffrey C. Neal², Karina Nielsen³, Paul D. Bates²,
Peter Bauer-Gottwein¹

¹Department of Environmental Engineering, Technical University of Denmark, Kgs. Lyngby, Denmark

²School of Geography, University of Bristol, Bristol, United Kingdom

³National Space Institute, Technical University of Denmark, Kgs. Lyngby, Denmark]

Contents of this file

Text S1

Figure S1

Tables S1 to S2

Introduction

The supporting information contains additional information concerning the in-situ data used for validation of the hydrological model, as well as a more detailed description of the mathematical equations used for the steady-state hydraulic solver.

Text S1.

The Saint-Venant equations express the mass balance and momentum balance equations for gradually varied one-dimensional flow in an open channel

$$\frac{\partial A}{\partial t} + \frac{dQ}{dx} = q \quad (C.1)$$

$$\frac{\partial Q}{\partial t} + \frac{\partial}{\partial x} \left(\frac{\beta Q^2}{A} \right) + gA \frac{\partial h}{\partial x} - gA(S_0 - S_f) = 0 \quad (C.2)$$

x is the chainage or distance along the channel [m], t the time [s], h the channel depth [m], Q the discharge [m^3/s], A , the flow cross-sectional area [m^2], q the lateral inflow [m^3/s], g , the acceleration due to gravity (set to $9.81 \text{ m}^2/\text{s}$) and β the momentum coefficient (set to unity). The bed slope, S_0 [m/m] is given by

$$S_0 = -\frac{dz}{dx} \quad (C.3)$$

z is the channel datum or bed elevation above a given height. The friction slope, S_f [m/m], is given by

$$S_f = \frac{Q^2}{K^2} \quad (C.4)$$

K , the conveyance [m^3/s], can be expressed as a function of channel cross-section geometry using Manning's equation

$$K = \frac{A^{5/2}}{n \times P^{3/2}} \quad (C.5)$$

P is the wetted perimeter [m] and n is Manning's friction coefficient [$\text{s}/\text{m}^{1/3}$].

If we assume steady flow, i.e., constant Q , and no lateral inflow, the mass balance equation (Eq. C.1) becomes equal to the lateral inflow and Saint-Venant equations simplify to

$$\frac{dh}{dx} - \frac{Q^2}{gA^3} \frac{dA}{dx} - S_0 + \frac{Q^2}{K^2} = 0 \quad (C.6)$$

By taking the partial derivative of the area relative to the chainage and width, and expanding the first term, Eq. C.2 becomes:

$$\left(1 - \frac{Q^2}{gA^3} \frac{\partial A}{\partial h} \right) \frac{dh}{dx} - \frac{Q^2}{gA^3} \frac{\partial A}{\partial x} - S_0 + \frac{Q^2}{K^2} = 0 \quad (C.7)$$

Isolating the change in depth over the chainage gives the general form of the equation to solve

$$\frac{dh}{dx} = \frac{\left(\frac{Q^2}{gA^3} \frac{\partial A}{\partial x} + S_0 - \frac{Q^2}{K^2} \right)}{\left(1 - \frac{Q^2}{gA^3} \frac{\partial A}{\partial h} \right)}$$

$$\frac{dh}{dx} = RHS(x, h(x)) \quad (C.8)$$

Where RHS (Right Hand Side) is the collection of terms not containing the derivative of the depth with respect to the chainage. We can replace $\frac{\partial A}{\partial h}$ and $\frac{\partial A}{\partial x}$ with channel properties. For a rectangular channel with variable width $w = w(x)$

$$\frac{dh}{dx} = \frac{\left(\frac{Q^2}{gA^3} \frac{dw}{dx} + S_0 - \frac{Q^2}{K^2} \right)}{\left(1 - \frac{Q^2}{gA^3} b \right)} \quad (C.9)$$

If we apply this method to larger river networks, there will be lateral inflow, q , at certain points. Therefore, we must take into account

$$\frac{d}{dx} \frac{Q^2}{A} = \frac{A \frac{dQ^2}{dx} - Q^2 \frac{dA}{dx}}{A^2} \quad (C.10)$$

$$\frac{dQ^2}{dx} = \frac{d(Q^2)}{dQ} \frac{dQ}{dx} = 2Q \times q \quad (C.11)$$

Eq. C11 becomes

$$\frac{dh}{dx} = \frac{\left(\frac{Q^2}{gA^3} \frac{\partial A}{\partial x} + S_0 - \frac{Q^2}{K^2} + \frac{2Q \times q}{gA^2} \right)}{\left(1 - \frac{Q^2}{gA^3} \frac{\partial A}{\partial h} \right)}$$

$$\frac{dh}{dx} = RHS(x, h(x)) \quad (C.12)$$

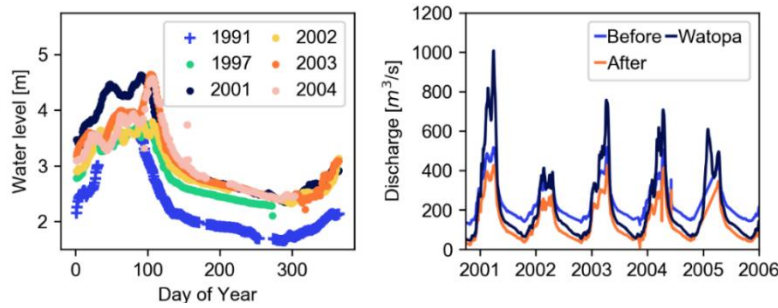


Figure S1. Water level at Kabompa Boma over the years of observation with at least 250 days of record and discharge record before and after bias correction of the level observations. The observed shift between the pre-1990 and post-2000s records is likely due to a shift in reference height, resulting in a bias of 65 cm. Comparison with the closest downstream station, Watopa, confirms this discrepancy. The station rating curve is applied to obtain the corrected post-2000 discharge records.

Main river and tributaries	Drainage area [km ²]	Length [km]/ tributary to	Observations	Stations	Time of operation	Mean annual discharge [m ³ /s]	CryoSat-2 observations after outlier removal
Zambezi	238,667	468.9	Discharge, stage	Chavuma (1105)	1959-2019	656	140
				Zambezi Pump house (1150)	1990-2006	911	
				Lukulu (2030)	1950-2018	886	
Kabompo	72,068	491.0		Kabompo Boma* (1650)	2000-2008	165	83
				Watopa (1950)	1958-2019	273	
Lungwebungo	47,071	754.1					375
Kafue	102,714	739,1	Discharge, stage	Chilenga (4350)	1962-2007	153	180
				M'Swebi (4435)	1953-2005	162	
				Lubungu (4450)	1959-2007	147	
				Hook Pontoon (4670)	1973-2008	231	
Lunga	24,517	Kafue		Chifumpa Pontoon (4560)	1959-2007	87	
Luangwa	149,523	989.4	Discharge, stage	Great East Rd. Bridge (5940)	1948-2002	168	230

Table S1. Summary of In-situ stations used to calibrate the hydrologic (discharge records) and validate the hydrodynamic model (stage records) and of the number of CryoSat-2 observations available for calibration of the hydraulic model are indicated for the three study areas. The mean annual discharge is over the time of simulation, 2001-2018. *: the discharge record at Kabompo Boma has been manually bias-corrected based on historical records from 1990-1992.

	Calibration zones	Calibration and validation stations	RMSD of discharge climatology	Flow duration curve	Non-parametric KGE
Upper Zambezi	1. Low slope, dominant forest cover	4. Watopa (C)	1. 0.63	1. 0.12	1. 0.82
	2. Low slope, land cover mosaic	5. Chavuma (C)	2. 1.05	2. 0.21	2. 0.74
	3. High slope, dominant forest cover	6. Kabompo Boma (C)	3. 0.79	3. 0.15	3. 0.84
Kafue	7. Low slope, forest cover > 75%	11. Lubungu (C)	1. 1.47	1. 0.08	1. 0.88
	8. Low slope, land cover mosaic	12. Hook Pontoon (C)	2. 0.83	2. -0.36	2. 0.87
	9. High slope, forest and shrub mosaic	13. Chilenga (C)	3. 0.57	3. -1.04	3. 0.90
	10. High slope, forest cover > 80%	14. Chifumpa Pontoon (C)	4. 1.64	4. -0.72	4. 0.74
Luangwa	15. High cover, forest mosaic	16. Great East Rd. Bridge (C)	1. 0.58	1. 0.002	1. 0.37

Table S2. Summary of calibration setup of the rainfall-runoff model and performance statistics at the calibration and validation stations